



**HAL**  
open science

# Isotopic Constraints on the Nature of Primary Precipitates in Archean–Early Paleoproterozoic Iron Formations from Determinations of the Iron Phonon Density of States of Greenalite and 2L- and 6L-Ferrihydrite

Andy W Heard, Nicolas Dauphas, Isaac L Hinz, Jena E Johnson, Marc Blanchard, Esen E Alp, Michael Y Hu, Jiyong Zhao, Barbara Lavina, Mark E Fornace, et al.

## ► To cite this version:

Andy W Heard, Nicolas Dauphas, Isaac L Hinz, Jena E Johnson, Marc Blanchard, et al.. Isotopic Constraints on the Nature of Primary Precipitates in Archean–Early Paleoproterozoic Iron Formations from Determinations of the Iron Phonon Density of States of Greenalite and 2L- and 6L-Ferrihydrite. ACS Earth and Space Chemistry, 2023, 10.1021/acsearthspacechem.2c00313 . hal-04044631

**HAL Id: hal-04044631**

**<https://hal.science/hal-04044631>**

Submitted on 24 Mar 2023

**HAL** is a multi-disciplinary open access archive for the deposit and dissemination of scientific research documents, whether they are published or not. The documents may come from teaching and research institutions in France or abroad, or from public or private research centers.

L'archive ouverte pluridisciplinaire **HAL**, est destinée au dépôt et à la diffusion de documents scientifiques de niveau recherche, publiés ou non, émanant des établissements d'enseignement et de recherche français ou étrangers, des laboratoires publics ou privés.

1 Isotopic constraints on the nature of primary  
2 precipitates in Archean-early Paleoproterozoic iron  
3 formations from determinations of the iron phonon  
4 density of states of greenalite, and 2L- and 6L-  
5 ferrihydrite.

6  
7 *Andy W. Heard<sup>1,2,3,\*</sup>, Nicolas Dauphas<sup>1</sup>, Isaac L. Hinz<sup>4</sup>, Jena E. Johnson<sup>4</sup>, Marc Blanchard<sup>5</sup>, Esen*  
8 *E. Alp<sup>6</sup>, Michael Y. Hu<sup>6</sup>, Jiyong Zhao<sup>6</sup>, Barbara Lavina<sup>6,7</sup>, Mark E. Fornace<sup>1,8</sup>, Justin Y. Hu<sup>1,9</sup>,*  
9 *Mathieu Roskosz<sup>10</sup>, Corliss Kin I Sio<sup>11</sup>, Nicole X. Nie<sup>12</sup>, Benoît Baptiste<sup>10</sup>.*

10 *\*Corresponding author: [andrew.heard@whoi.edu](mailto:andrew.heard@whoi.edu)*

11  
12 <sup>1</sup>Origins Laboratory, Department of the Geophysical Sciences and Enrico Fermi Institute, The  
13 University of Chicago, Chicago, IL 60637, USA.

14 <sup>2</sup>Department of Geology & Geophysics, Woods Hole Oceanographic Institution, Woods Hole,  
15 MA 02536, USA.

16 <sup>3</sup>NIRVANA Laboratories, Woods Hole Oceanographic Institution, Woods Hole, MA, 02536  
17 USA.

18 <sup>4</sup>Department of Earth and Environmental Sciences, University of Michigan, 1100 North  
19 University Avenue, Ann Arbor, MI 48109, USA.

20 <sup>5</sup>Géosciences Environnement Toulouse (GET), Observatoire Midi-Pyrénées,s, CNRS, IRD,  
21 CNES, UPS, 14 Avenue Edouard Belin, Toulouse 31400, France.

22 <sup>6</sup>Advanced Photon Source, Argonne National Laboratory, 9700 South Cass Avenue, Argonne, IL  
23 60439, USA.

24 <sup>7</sup>Center for Advanced Radiation Sources, The University of Chicago, Chicago, IL 60439, USA

25 <sup>8</sup>Division of Chemistry & Chemical Engineering, California Institute of Technology, Pasadena,  
26 CA 91125, USA.

27 <sup>9</sup>Department of Earth Sciences, University of Cambridge, Downing Street, Cambridge CB2 3EQ,  
28 UK.

29 <sup>10</sup>Institut de Minéralogie, de Physique des Matériaux et de Cosmochimie, Sorbonne Université, 4  
30 Place Jussieu, Paris 75005, France.

31 <sup>11</sup>Department of Earth Sciences, University of Toronto, Ontario, Canada

32 <sup>12</sup>The Isotoparium, Division of Geological and Planetary Sciences, California Institute of  
33 Technology, Pasadena, CA 91125, USA.

34

35 **KEYWORDS**

36 Iron Formations

37 Iron Isotopes

38 Greenalite

39 Ferrihydrite

40 Great Oxidation Event

41 Iron phonon density of states

42 **ABSTRACT (249 words)**

43 Iron formations (IFs) are chemical sedimentary rocks that were widely deposited before the Great  
44 Oxidation Event (GOE) at 2.4-2.2 Ga. It is generally thought that IFs precipitated as hydrated Fe<sup>3+</sup>  
45 oxides (HFOs) such as ferrihydrite following surface oxidation of Fe<sup>2+</sup>-rich, anoxic deep waters.  
46 This model often implicates biological oxidation and underpins reconstructions of marine nutrient  
47 concentrations. However, nanoscale petrography indicates that an Fe<sup>2+</sup> silicate, greenalite, is a  
48 common primary mineral in well-preserved IFs, motivating an alternative depositional model of  
49 anoxic ferrous silicate precipitation. It is unclear however if Fe<sup>2+</sup>-rich silicates can produce the Fe  
50 isotopic variations in IFs that are well explained by Fe<sup>2+</sup> oxidation. To address this question, we  
51 constrain the equilibrium Fe isotopic (<sup>56</sup>Fe/<sup>54</sup>Fe) fractionation of greenalite and ferrihydrite, by  
52 determining the iron phonon densities of states for those minerals. We use *ab initio* Density  
53 Functional Theory (DFT + *U*) calculations and Nuclear Resonant Inelastic X-Ray Scattering  
54 (NRIXS) spectroscopy, to show that ferrous greenalite should be isotopically lighter than  
55 ferrihydrite by ~1-1.2 ‰ at equilibrium, and fractionation should scale linearly with increasing  
56 Fe<sup>3+</sup> content in greenalite. By anchoring ferrihydrite-greenalite mineral pair fractionations to  
57 published experimental Fe isotopic fractionations between HFOs and aqueous Fe<sup>2+</sup>, we show that  
58 ferrous greenalite may produce all but the heaviest pre-GOE Fe isotopic compositions and mixed  
59 valence greenalites can produce the entire record. Our results suggest that heavy Fe isotope  
60 enrichments are not diagnostic of primary IF mineralogies, and ferrihydrite, partially oxidized or  
61 even purely ferrous greenalite are all viable primary mineralogies IFs.

62 **MAIN TEXT (9312 words)**

63 **1. INTRODUCTION**

64 Until ~2.43 billion years ago (Ga), Earth's atmosphere was practically devoid of free oxygen (O<sub>2</sub>)<sup>1–</sup>  
65 <sup>3</sup>. Prior to the Great Oxidation Event (GOE) beginning around 2.43 Ga, and for substantial periods  
66 of time after it, the oceans were largely anoxic<sup>4</sup>, and had high concentrations of dissolved Fe<sup>2+</sup> and  
67 silica (SiO<sub>2(aq)</sub>). The large marine Fe<sup>2+</sup> pool was likely sourced predominantly from seafloor  
68 hydrothermal vents<sup>5–9</sup>, with contributions from anoxic continental weathering<sup>6,10,11</sup>. Widespread  
69 iron formations (IFs), distinctive chemical sedimentary rocks rich in Fe and Si, are a hallmark of  
70 pre-GOE sedimentary rocks (Fig. 1)<sup>6,12–14</sup>. Most IFs preceding the GOE are banded iron formations  
71 (BIFs), characterized by compositional layering at scales ranging from sub-mm rhythmic  
72 microbands of alternating Fe-rich and silica-rich minerals, to meter-scale macrobands defining  
73 facies transitions during major accumulations over millions of years (Fig. 1)<sup>15</sup>. The mineralogy of  
74 IFs is diverse, and can be broadly categorized into oxides dominated by magnetite [Fe<sub>3</sub>O<sub>4</sub>] and  
75 hematite [Fe<sub>2</sub>O<sub>3</sub>], Fe-rich carbonates, and the Fe silicates greenalite [(Fe<sup>2+</sup>, Fe<sup>3+</sup>)<sub>2–3</sub>Si<sub>2</sub>O<sub>5</sub>(OH)<sub>4</sub>],  
76 minnesotaite [Fe<sub>3</sub>Si<sub>4</sub>O<sub>10</sub>(OH)<sub>2</sub>] and stilpnomelane [K(Fe<sup>2+</sup>, Mg, Fe<sup>3+</sup>)<sub>8</sub>(Si, Al)<sub>12</sub>(O, OH)<sub>27</sub>·n(H<sub>2</sub>O)],  
77 all accompanied by ubiquitous chert (SiO<sub>2</sub>). The precursors to these minerals were precipitated  
78 from ancient oceans, but it is widely recognized that the present-day mineralogy of IFs is almost  
79 entirely secondary in nature—a result of prolonged early and late diagenesis, metamorphism, and  
80 interactions with fluids over their several-billion year histories<sup>13,14,16</sup>. The canonical interpretation  
81 is that the primary precipitates were amorphous silica and hydrous ferric oxides (HFOs), with the  
82 latter formed through the oxidation of Fe<sup>2+</sup> and rapid precipitation of insoluble Fe<sup>3+</sup> as  
83 oxyhydroxide phases<sup>17</sup>. Possible oxidants for Fe<sup>2+</sup> include O<sub>2</sub> (produced by early-evolved  
84 cyanobacteria)<sup>17</sup>, UV photons<sup>18–20</sup>, and direct Fe<sup>2+</sup> oxidation by anoxygenic photosynthesis<sup>21–23</sup>,

85 all of which would most likely have operated in the photic zone and thus restrict Fe precipitation  
86 to shallower waters supplied with  $\text{Fe}^{2+}$  upwelled from depth.

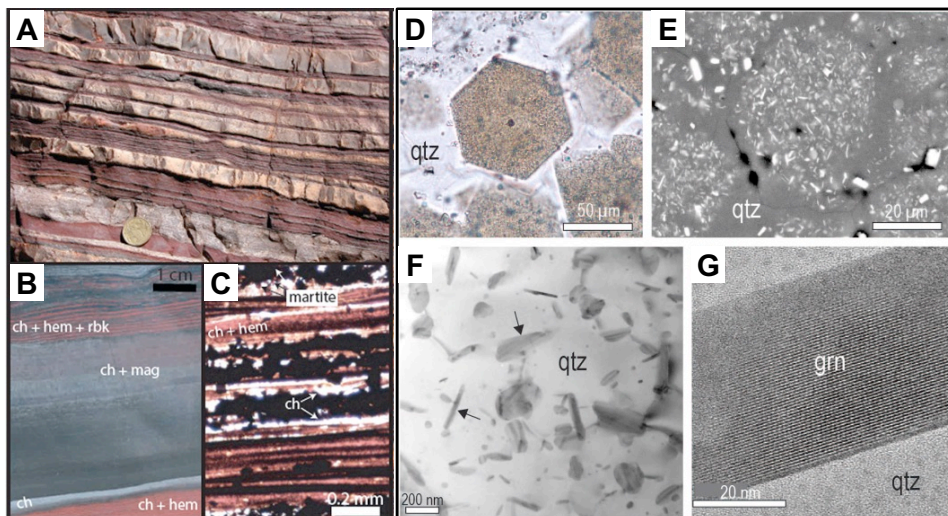


**Figure 1.** Images of pre-GOE iron formations (IFs) at various scales. **A.** Centimeter scale banding in the Joffre Member of the 2.46 Ga Brockman IF, in the Hamersley basin, Australia. **B.** Micro- and mesobanding, with chert, hematite, and riebeckite, microbanded layers and thicker chert and magnetite layers in the Joffre Member. **C.** Photomicrograph showing thin chert-hematite microbands, and coarser magnetite microbands (thick black layers) in the Joffre Member. **D.** Photomicrograph of greenalite-rich hexagonal chert pod surrounded by Fe-poor chert, from the 2.48 Ga Klein Naute Formation, Griqualand West Basin South Africa. **E.** Backscattered electron image from the 2.56 Ga Bee Gorge Member, Witenoom Formation, Hamersley basin, Australia. **F.** Bright-field transmission electron microscope (TEM) image from the Bee Gorge Member. **G.** High-resolution TEM image of greenalite nano particles, from the 2.56 Ga Bee Gorge Member. Images **A-C** from [Konhauser et al. Iron Formations: A Global Record of Neoproterozoic to Palaeoproterozoic Environmental History. \*Earth-Science Reviews\*. 2017, 172, 140–177. Copyright \(2017\) Elsevier.](#) Images **D-G** from [Rasmussen et al. Greenalite and Its Role in the Genesis of Early Precambrian Iron Formations – A Review. \*Earth-Science Reviews\*. 2021, 103613. Copyright \(2021\) Elsevier.](#)

87  
88 While IFs contain appreciable  $\text{Fe}^{3+}$ , they have an average Fe valence state of  $\sim 2.4+$  (60%  $\text{Fe}^{2+}$  and  
89 40%  $\text{Fe}^{3+}$ )<sup>16</sup>. This is evident both at the bulk scale, where IFs contain a variety of ferric and ferrous  
90 minerals, and in mixed-valence Fe minerals like magnetite [ $\text{Fe}^{3+}_2\text{Fe}^{2+}\text{O}_4$ ]. In the HFO model, much  
91 of the  $\text{Fe}^{2+}$  content in IFs is attributed to early or late diagenetic reduction of  $\text{Fe}^{3+}$  during the  
92 oxidation of organic matter, such as through microbial dissimilatory  $\text{Fe}^{3+}$  reduction (DIR) or

93 metasomatic reactions during burial heating<sup>24–28</sup>. The Fe<sup>2+</sup> produced by these reactions may have  
94 reacted with the remaining HFOs to form magnetite, or precipitated directly as Fe carbonate  
95 (siderite) or Fe<sup>2+</sup> silicates as early diagenetic phases<sup>14,29–31</sup>. Organic carbon is present in very low  
96 abundance in IFs<sup>32</sup>, possibly because it was respired away by reduction of excess Fe<sup>3+</sup>.

97

98 Assumptions related to the Fe<sup>2+</sup> oxidation model for IFs underpin most interpretations of the  
99 chemistry of the oceans prior to the GOE. The model prescribes an oceanic redox structure  
100 characterized by reducing deep marine basins enriched in Fe<sup>2+</sup> sourced from hydrothermal vents,  
101 and near-surface waters that were sufficiently oxidizing to precipitate HFOs. This primary  
102 precipitation of HFOs is also a key assumption of approaches used to quantitatively estimate  
103 concentrations of key nutrient elements in the Precambrian oceans from the geochemical archive  
104 of IFs<sup>33–38</sup>. These studies used experimentally calibrated nutrient element partitioning on HFOs to  
105 estimate seawater concentrations from geochemical analyses of IFs, most notably for phosphorous  
106 (P)<sup>33,34,37</sup>, the main limiting macronutrient over geological timescales, and nickel (Ni)<sup>35,36</sup>, a critical  
107 co-factor for methanogenesis.

108

109 Recently, the HFO model for IFs has been challenged by an alternative hypothesis in which the  
110 precursor mineralogy for Archean IFs and Fe-oxide-rich cherts was entirely composed of  
111 nominally Fe<sup>2+</sup>-dominated hydrous silicates, such greenalite Fe<sup>2+</sup><sub>3</sub>Si<sub>2</sub>O<sub>5</sub>(OH)<sub>4</sub>, with other Fe<sup>3+</sup>  
112 phases such as oxides and mixed-valence silicates reflecting late oxidative metamorphic  
113 overprints<sup>39–43</sup>. This new model for IF precursors is founded on a growing number of nanoscale  
114 observations of chert bands and nodules in IFs from 3.5–2.4 Ga and predominantly in the  
115 Hamersley Basin of Western Australia and the Transvaal Basin of South Africa that suggest Fe

116 silicates, not Fe-oxides, are the earliest-formed surviving minerals in IFs<sup>43-47</sup>. Nanoscale imaging  
117 techniques and elemental mapping in those studies specifically targeted chert bands and nodules  
118 where early diagenetic silicification preserved delicate microstructures shortly after deposition  
119 (Fig. 1D-G). These inclusions were identified as abundant nanoscale (10 nm × 200-1000 nm)  
120 particles of greenalite<sup>47,48</sup>. The endmember interpretation of this primary greenalite mineralogy  
121 requires that the oceans were fully anoxic during IF deposition, with Fe<sup>2+</sup> greenalite being the  
122 dominant mode of primary Fe precipitation in an ocean without the formation of insoluble Fe<sup>3+</sup>  
123 phases<sup>40,45</sup>.

124  
125 While greenalite has the nominal chemical formula Fe<sup>2+</sup><sub>3</sub>Si<sub>2</sub>O<sub>5</sub>(OH)<sub>4</sub> it can contain appreciable  
126 structural Fe<sup>3+</sup>, as a result of natural syn- and post-depositional processes<sup>39</sup>. A more nuanced  
127 picture comes from analysis of the redox state of Fe in greenalite in IFs. Using synchrotron-based  
128 Fe L-edge X-ray absorption spectroscopy (XAS) to determine the Fe<sup>3+</sup>/Fe<sub>tot</sub> (Fe<sub>tot</sub> = total Fe) ratio  
129 in individual greenalite grains in well-preserved 2.5 Ga IFs, greenalite nanoparticles were found  
130 to have Fe<sup>3+</sup> content of 10-20 % of their total Fe<sup>39</sup>. If the Fe<sup>3+</sup> in these minerals reflects primary  
131 incorporation of Fe<sup>3+</sup> formed in the ancient water column, this would relax the endmember ‘zero  
132 oxidation’ greenalite interpretation that the pre-GOE oceans were devoid of Fe<sup>2+</sup> oxidants, and  
133 allow for the partial oxidation of Fe<sup>2+</sup> during IF deposition<sup>39</sup>. Regardless of whether the silicates  
134 were entirely ferrous or a ferrous-ferric mix, if the precursor material for IFs prior to the GOE was  
135 dominated by silicates, then reconstructions of marine nutrient concentrations based on HFO  
136 adsorption experiments may be incorrect, and revision of these estimates would require similar  
137 adsorption experiments to be conducted with relevant authigenic silicates.

138



139 Given the major implications of primary IF precipitates for our understanding of early marine  
140 chemistry, a diagnostic tool that can distinguish between different precursor phases for IFs would  
141 be valuable for confirming or ruling out endmember models. Iron isotope geochemistry potentially  
142 has this elucidative capability. Iron isotopes are strongly fractionated at low temperature by redox  
143 processes and they are resistant to resetting by metamorphism, thus preserving primary  
144 sedimentary signals in ancient rocks with complex histories (specifically demonstrated for IFs by  
145 Frost et al.<sup>49</sup>). Furthermore, an extensive archive of Fe isotopic measurements of IFs and Fe-oxide-  
146 rich cherts spanning > 3 Ga of Earth history is readily available to test different IF precursor  
147 hypotheses (Fig. 2)<sup>50,51</sup>. IFs show large variations in the isotopic composition of Fe at bulk rock  
148 and mineral scales. The most striking Fe isotopic feature of IFs pre-dating the Great Oxidation  
149 Event (GOE) is the prevalence of highly positive  $\delta^{56}\text{Fe}$  values. These positive values have long  
150 been taken as evidence for partial  $\text{Fe}^{2+}$  oxidation in the Archean oceans, because oxidation induces  
151 a strong fractionation in Fe isotopes that partitions isotopically heavy Fe into  $\text{Fe}^{3+}$  relative to  $\text{Fe}^{2+}$ .  
152 Even the most ancient IF occurrences from Isua (SW Greenland) and Nuvvuagittuq (Québec,  
153 Canada) (~3.7-3.8 Ga) are characterized by clear heavy Fe isotopic enrichments<sup>52-54</sup>, while  
154 younger IFs spanning the Archean and early Paleoproterozoic up to the GOE exhibit a wide range  
155 of heavy and light Fe isotopic enrichments<sup>51</sup>.

156  
157 The partial oxidation interpretation of the IF Fe isotope record is supported by numerous examples  
158 in experiments, and nature, of heavy Fe isotopic enrichment during the oxidation of  $\text{Fe}^{2+}$  to HFOs.  
159 The  $\delta^{56}\text{Fe}$  of the solid HFO phase can be shifted heavier by 1-3 ‰ relative to the  $\text{Fe}^{2+}$  in  
160 solution<sup>20,55-59</sup>. Meanwhile, experimental precipitation of  $\text{Fe}^{2+}/\text{Fe}^{3+}$  green rusts and the Fe  
161 carbonate siderite found a small Fe isotopic fractionation between dissolved and precipitated  $\text{Fe}^{2+}$

162 that enriched most solids in the lighter Fe isotopes<sup>60</sup>. The green rust and siderite experiments thus  
 163 revealed that these phases cannot account for isotopically heavy Fe in IFs. The most parsimonious  
 164 interpretation for the heavy Fe isotope enrichments measured in Archean IFs and Fe-oxide-rich  
 165 cherts (up to +2.6 ‰)<sup>51,61</sup> is therefore that they formed by partial Fe oxidation<sup>50,51</sup>. The entire Fe  
 166 isotopic record of IFs can then be explained through partial oxidation, and progressive distillation  
 167 of an Fe<sup>2+</sup> reservoir during upwelling.  
 168

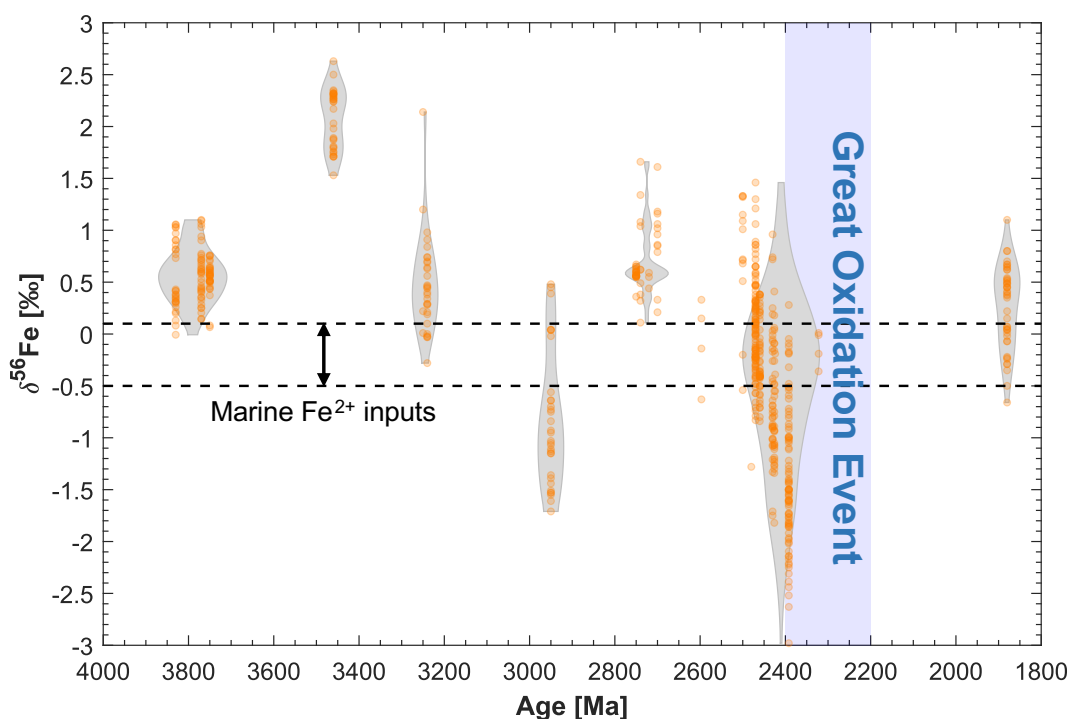


**Figure 2.** The Fe isotopic record of Archean and Paleoproterozoic iron formations (IFs) and Fe-oxide-rich cherts (modified from Heard and Dauphas, 2020).  $\delta^{56}\text{Fe}$  is the per mil ‰ deviation in the  $^{56}\text{Fe}/^{54}\text{Fe}$  ratio of samples relative to a standard material, IRMM-014 that is isotopically similar to the bulk Earth. Orange circles show individual datapoints. Grey shaded fields (violin plots) show the kernel density of  $\delta^{56}\text{Fe}$  values in 200-million-year time bins centered on the major IFs throughout the Archean and Paleoproterozoic, where the relative width of violin plots is not to scale.

169 The extent of equilibrium isotopic fractionations between precipitated minerals put forward as IF  
 170 precursors and dissolved Fe<sup>2+</sup> remain uncertain. While prior experiments have informed a general

171 expectation for the Fe isotopic behaviors of authigenic ferrous phases, the lack of data for  
172 Fe<sup>2+</sup>-bearing minerals such as greenalite stems in part from the difficulty of running equilibration  
173 experiments for minerals that are readily oxidized under modern atmospheric conditions. Another  
174 limitation of bulk precipitation experiments is that they can be affected by both equilibrium and  
175 kinetic processes. It is therefore important and timely to constrain the equilibrium Fe isotopic  
176 fractionation behavior of greenalite relative to ferrihydrite, and dissolved Fe<sup>2+</sup>. To do this, we  
177 employed a combined experimental and computational approach that has proven to be powerful in  
178 determining the equilibrium Fe isotopic behavior of other Fe-bearing minerals with relevance to  
179 low temperature geochemistry<sup>62,63</sup>.

180

## 181 **2. MATERIALS AND METHODS**

### 182 *2.1 General approach*

183 Our principal objective is to determine the reduced partition function ratios (also called  $\beta$  factors)  
184 for the materials of interest. The  $\beta$  factors for two phases  $a$  and  $b$  can be used to determine the  
185 equilibrium isotopic fractionation factor  $1000 \ln \alpha_{a-b}$  (in ‰) between them,

$$186 \quad 1000 \ln \alpha_{a-b} = 1000 \ln \beta_a - 1000 \ln \beta_b. \quad (1)$$

187 We use a two-pronged approach that combines *ab initio* computations of mineral structures, and  
188 nuclear resonant inelastic X-ray scattering (NRIXS), a synchrotron spectroscopic technique, to  
189 determine  $\beta$  factors. The use of two independent techniques provides a consistency check and this  
190 approach has been applied effectively in earlier works<sup>62,64</sup>.

191

192 It is nontrivial to calculate the equilibrium fractionation between solid and dissolved species. Iron  
193 isotopic fractionations between aqueous and minerals directly calculated using Fe  $\beta$  factors from

194 a combination of *ab initio* simulations (fluids, minerals) and NRIXS measurements (minerals)  
195 have the potential to introduce biases associated with their respective computational methods  
196 (Dauphas et al.<sup>50</sup> and references therein). Early computational methods used to calculate  
197 theoretical Fe  $\beta$  factors for aqueous species<sup>65</sup> have indicated equilibrium fractionations between  
198 Fe(II) and Fe(III) that are up to ~2 times those directly observed in Fe isotope equilibration  
199 experiments<sup>66,67</sup>; although more recent computations do find better agreement with empirical  
200 experiments<sup>68-72</sup>. However, when *ab initio* data for aqueous species are combined with *ab initio*  
201 data for mineral species or NRIXS data for mineral species, the calculated  $\beta$  factors fail to  
202 reproduce the measured fractionation from fluid-mineral equilibration experiments<sup>63,68-73</sup>. This  
203 disagreement appears to derive predominantly from study-to-study variations in the absolute  $\beta$   
204 factor for Fe(III)<sub>aq</sub><sup>50</sup>.

205  
206 The approach recommended by Dauphas et al.<sup>50</sup> to mitigate these potential biases is to calculate  
207 the fractionation factors between different minerals and Fe(II)<sub>aq</sub> by using mineral-pair equilibrium  
208 isotopic fractionations, which are derived from NRIXS or *ab initio* approaches, wherein one  
209 mineral in the pair is a reference mineral for which fluid-mineral isotopic equilibration has been  
210 directly measured. Here, we take ferrihydrite as the reference mineral in order to calculate the  
211 equilibrium Fe(II)<sub>aq</sub>-greenalite fractionation factor that is of interest to understanding the origin of  
212 Archean IFs. The fractionation during ferrihydrite (or similar HFO) equilibration with, or  
213 precipitation from, Fe(II) solutions has been constrained in numerous studies<sup>20,55-59,66,67,74,75</sup>, thus  
214 making it a suitable reference phase in calculating the equilibrium Fe isotopic fractionation  
215 associated with greenalite precipitation.

216

217 Establishing an understanding of the equilibrium isotopic behavior of a mineral phase is the first  
218 step in interpreting isotopic fractionation in natural systems because only a few data are needed  
219 (nature of the minerals/aqueous species and temperature) to predict equilibrium fractionations  
220 between phases. Deviations from the null equilibrium hypothesis can then be attributed to kinetic  
221 and/or reservoir effects, which require additional data (mineral zoning, thermal history) to  
222 constrain.

223

## 224 *2.2. Sample materials for NRIXS*

### 225 *2.2.1. Natural greenalite*

226 A sample of a natural greenalite standard from the San Valentin Ore Body, Murcia, Spain<sup>76</sup> was  
227 used for NRIXS analysis. This is, to our knowledge, the naturally occurring greenalite sample with  
228 the lowest level of contaminant minerals. After crushing of the rock standard, a greenalite separate  
229 was obtained by hand-picking and its identification was confirmed with X-ray diffraction (XRD)<sup>39</sup>.  
230 Aliquots of this material have previously been employed as a greenalite standard for XAS  
231 investigation of Fe redox states in IF-hosted greenalite<sup>39</sup>. All sample preparation took place on  
232 benchtop as the standard was known to be stable in air.

233

### 234 *2.2.2. Ferrihydrite*

235 Ferrihydrite samples doped in <sup>57</sup>Fe were synthesized in a modified protocol following  
236 Schwertmann and Cornell<sup>77</sup>, with some departures necessary due to the use of <sup>57</sup>Fe metal rather  
237 than Fe(NO<sub>3</sub>)<sub>3</sub> as starting material. Both 2-line (1-3 nm crystallite size) and 6-line (5-6 nm  
238 crystallite size) ferrihydrite were synthesized. All aqueous solutions were prepared with MilliQ  
239 water (MQ; 18 MΩ). For 2-line ferrihydrite, 85.6 mg of <sup>57</sup>Fe (95%, Cambridge Isotope

240 Laboratories) was dissolved in 3 mL 15.4 M HNO<sub>3</sub> at 100° C for 3 days. The solution was allowed  
241 to cool to 25° C, then rapidly titrated with ~30 mL of a 1.5 M NaOH solution to pH 7.0, all while  
242 vigorously stirring. The precipitate was collected by centrifuging 10 times at 10-fold dilutions in  
243 MQ (10<sup>10</sup> theoretical dilution overall), followed by drying under a fume hood at 25° C. For 6-line  
244 ferrihydrite, 56.5 mg of <sup>57</sup>Fe was dissolved in 1.5 mL 11 M HClO<sub>4</sub> at 100°C for 2 days. The  
245 solution was partially evaporated at 110° C and refilled with 11 M HClO<sub>4</sub>. This process was  
246 repeated 5 times. The solution was evaporated completely at 110°C. The resultant salt was  
247 dissolved in 40 mL MQ at 75° C for 10 minutes, then cooled to 25° C in an ice bath. The solution  
248 was continuously dialyzed with MQ for 10 days, then freeze dried to isolate the solid.

249  
250 Characterization of the powders to ensure that 2-line and 6-line ferrihydrite were produced by the  
251 syntheses described above was done by XRD and TEM analysis (Fig. 4). X-ray powder diffraction  
252 measurements were carried out at the XRD platform of the IMPMC (Paris, France) in transmission  
253 geometry, on a Rigaku MM007HF diffractometer equipped with a Mo rotating anode source  
254 ( $\lambda K\alpha_1 = 0.709319 \text{ \AA}$ ,  $\lambda K\alpha_2 = 0.713609 \text{ \AA}$ ), Varimax focusing optics and a RAXIS4++ image plate  
255 detector. LaB6 standard sample was measured in the same experimental conditions to calibrate the  
256 FIT2D program<sup>78</sup>, the image processing software used to integrate the intensities around the  
257 Debye–Scherrer rings. We performed additional characterization by HR-TEM and selected area  
258 electron diffraction (SAED) (Figs. 4C-D). Images were obtained using a FEI Tecnai F30 at 300  
259 kV with a point-to-point resolution of 0.2 nm. TEM samples were prepared using the methods of  
260 Janney et al.<sup>79</sup> and placed on porous carbon grids.

261

262 *2.3. NRIXS analysis of greenalite and ferrihydrite*

263 NRIXS analyses were conducted at Sector 3-ID of the Advanced Photon Source (APS)  
264 synchrotron beamline at Argonne National Laboratory in Lemont, IL, USA. NRIXS is a relatively  
265 new spectroscopic technique<sup>80,81</sup> that can be used to probe the vibrational properties of select  
266 Mössbauer elements in solids. In the case of Fe, NRIXS is effective because <sup>57</sup>Fe is a Mössbauer  
267 isotope that has a low-lying nuclear excited state at 14.4125 keV. The lifetime of the excited  
268 nuclear state is 141 ns for <sup>57</sup>Fe, which is long relative to both the duration of electronic scattering  
269 of most X-rays (< 1 ps), and the duration of pulsed X-ray flashes provided by the synchrotron  
270 source (70 ps pulses, separated by 153 ns). As such, nuclear resonance enables time discrimination  
271 to isolate the energy scattering spectrum caused by nuclear transitions.

272  
273 The vibrational properties of Fe in solids can be probed with the nuclear scattering spectrum.  
274 Recoilless elastic scattering produces part of the signal. The remaining inelastic portion of the  
275 scattering signal is influenced by the material lattice holding Fe atoms in place. The inelastic  
276 scattering spectrum spans a far broader energy range (on the order of +/- 100 meV) than the  
277 linewidth of the nuclear transition. When an incident photon has a higher energy than the low-  
278 lying excited state of the <sup>57</sup>Fe nucleus, excess energy can be dispersed to the solid material lattice  
279 by excitation of quantized modes of vibration called phonons (phonon creation). Conversely,  
280 X-rays with an energy slightly below that required for the nuclear transition can excite nuclei as  
281 well, with vibration in the mineral lattice providing the extra energy (phonon annihilation). After  
282 removing the central elastic peak associated with absorption by X-rays at the resonant energy,  
283 NRIXS enables probing of the full vibrational spectrum of <sup>57</sup>Fe in solids as a function of energy,  
284 called the partial phonon density of states (pDOS), or  $g(E)$ , being ‘partial’ because only the  
285 vibrational properties of Fe in the lattice are determined<sup>81</sup>. We can determine  $\beta$  factors either by

286 taking the moments of  $g(E)$ , or the energy scattering spectrum  $S(E)$ <sup>63,82</sup>. In the case of  $S(E)$ , the  
 287 formula to determine  $\beta$  factors is,

$$288 \quad 1000 \ln \beta \approx 1000 \left( \frac{M}{M^*} - 1 \right) \frac{1}{E_R} \left[ \frac{R_3^S}{8k^2T^2} - \frac{R_3^S - 10R_2^S R_3^S}{480k^4T^4} + \frac{R_7^S + 210(R_2^S)^2 R_3^S - 35R_3^S R_4^S - 21R_2^S R_5^S}{20160k^6T^6} \right], \quad (2)$$

289 where  $M$  and  $M^*$  are the masses of two isotopes of interest (*e.g.* 56 and 54),  $E_R$  is the free recoil  
 290 energy (1.956 meV for <sup>57</sup>Fe),  $T$  is the temperature,  $k$  is the Boltzmann constant, and  $R_i^S$  is the  $i^{\text{th}}$   
 291 centered moment of the scattering spectrum  $S(E)$  where  $R_i^S = \int_{-\infty}^{+\infty} S(E)(E-E_R)^i dE$ . The equation  
 292 relating  $1000 \ln \beta$  to  $S(E)$  was derived by Dauphas et al.<sup>63</sup> and Hu et al.<sup>82</sup>. One can use a  
 293 mathematically equivalent expression for  $g(E)$  to determine  $1000 \ln \beta$ <sup>63,82,83</sup>,

$$294 \quad 1000 \ln \beta \approx 1000 \left( \frac{M}{M^*} - 1 \right) \frac{1}{E_R} \left[ \frac{m_2^g}{8k^2T^2} - \frac{m_4^g}{480k^4T^4} + \frac{m_6^g}{20160k^6T^6} \right], \quad (3)$$

295 Where  $m_j^g$  is the  $j^{\text{th}}$  moment of the pDOS  $g(E)$  where  $m_j^g = \int_0^{+\infty} E^j g(E) dE$ . As discussed by Dauphas  
 296 et al.<sup>63</sup>, the two formulas are mathematically equivalent but  $g$  is calculated by taking a Fourier-Log  
 297 transform of  $S$ <sup>81</sup>. Error assessment is therefore more complicated<sup>62</sup>. Equations 2 and 3 for  $1000 \ln \beta$   
 298 fit the general expected functional form for  $\beta$  factors of,

$$299 \quad 1000 \ln \beta \approx \frac{A_1}{T^2} + \frac{A_2}{T^4} + \frac{A_3}{T^6}, \quad (4)$$

300 where  $A_1$ ,  $A_2$ , and  $A_3$  can be calculated from Equation 2, above.

301 Alternatively,  $1000 \ln \beta$  can be expressed as a more compact function of the force constant  $\langle F \rangle$ :

$$302 \quad 1000 \ln \beta \approx \frac{B_1 \langle F \rangle}{T^2} + \frac{B_2 \langle F \rangle^2}{T^4}, \quad (5)$$

303 where  $B_1$  is 2904,  $B_2$  is a constant that depends on the pDOS  $g$ , and the mean force constant  $\langle F \rangle$   
 304 of bonds that hold Fe in position is given by

$$305 \quad \langle F \rangle = \frac{M}{E_R \hbar^2} R_3^S, \quad (6)$$



306 where  $\hbar$  is the reduced Planck's constant. The equation for  $1000\ln\beta$  can be reduced to just the first  
307 term at high temperature. Additionally, Dauphas et al.<sup>63</sup> showed that using a fixed value of 52000  
308 for  $B_2$  introduces less than 0.2 % error at 22 °C, which is smaller than the overall uncertainty of  
309 the NRIXS method. While we use the full polynomial expansion (Eqs. 2, 4) to calculate the  
310 temperature-dependence of the  $\beta$ -factors, we will initially describe our results in terms of the force  
311 constant  $\langle F \rangle$  as it is more straightforward to compare a single parameter and this still captures most  
312 of the systematics of interest.

313  
314 NRIXS data were collected by scanning in 0.25 meV steps around the nominal resonance energy  
315 using a set of high-resolution monochromators. Scattered X-rays were measured with avalanche  
316 photo-diodes (APDs). Natural greenalite and synthesized ferrihydrite were analyzed in different  
317 sessions. The natural greenalite sample was scanned over -164 to +164 meV relative to the elastic  
318 peak. The 2-line and 6-line ferrihydrite sample powders were scanned over the range -160 to +160  
319 meV relative to the elastic peak. Broad energy scans are used to monitor count rates in the tails of  
320 the distribution used for background corrections<sup>84</sup>. Because the synthesis protocol enabled  
321 ferrihydrite samples to be prepared with <sup>57</sup>Fe-enriched material, they provided stronger signals,  
322 and 5 and 7 scans were made for 2-line and 6-line ferrihydrite, respectively. The greenalite  
323 contained Fe with natural isotopic abundances, so the concentration of <sup>57</sup>Fe was much smaller, and  
324 more scans were needed. For the natural greenalite, 14 scans were made. Additionally,  $\text{Fe}^{3+}/\text{Fe}_{\text{total}}$   
325 in the natural greenalite standard was determined prior to NRIXS analysis using nuclear forward  
326 scattering<sup>85,86</sup>, wherein the synchrotron signal was used in place of a traditional Mössbauer source  
327 to determine the Mössbauer spectrum of the material in the time domain (Synchrotron Mössbauer  
328 Spectroscopy - SMS<sup>87</sup>; Fig. 5).

329

330 All NRIXS data were reduced in Mathematica using the SciPhon<sup>84</sup> program designed for this  
331 purpose. The SciPhon software outputs many other parameters from the phonon excitation  
332 probability density function  $S(E)$  and the PDOS  $g(E)$ , such as the Lamb-Mössbauer factor,  
333 Helmholtz free energy, and vibrational entropy. The values of these parameters are made available  
334 in Supplementary Table S1 for future use.

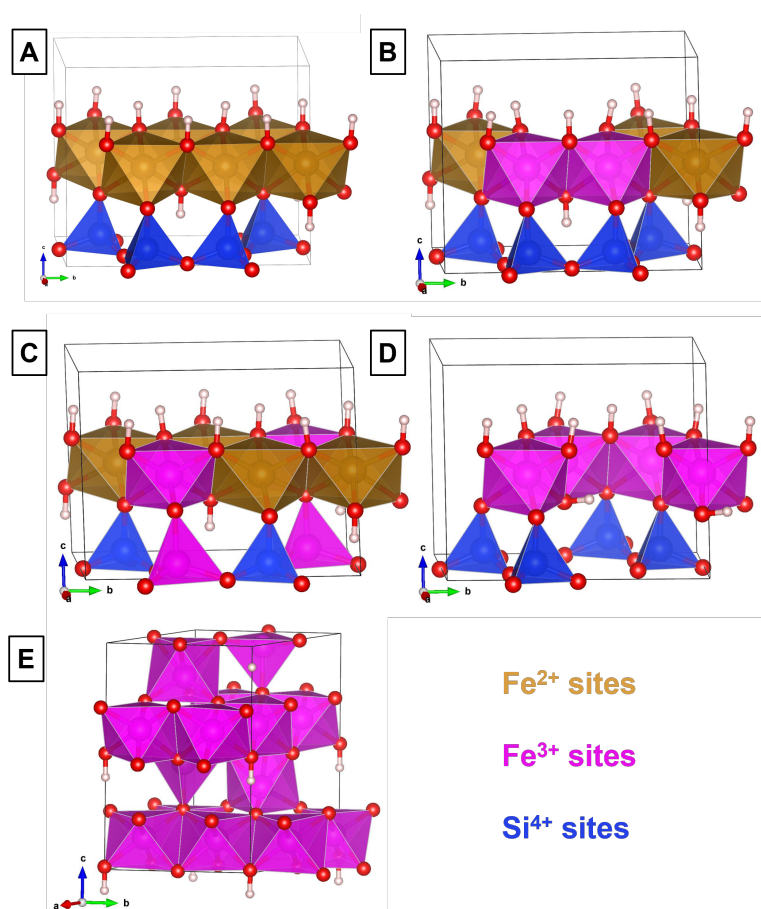


**Fig. 3:** Crystal structures optimized by DFT+ $U$ , for **A:** Fe<sup>2+</sup> greenalite (Gruner, 1936). **B:** Fe<sup>2.4+</sup> greenalite, constructed assuming a vacancy substitution in 1/6 of octahedral sites ( $6\text{Fe}^{2+} \leftrightarrow 3\text{Fe}^{2+}2\text{Fe}^{3+}\square$ ). **C:** Fe<sup>2.5+</sup> greenalite, constructed assuming a ferri-Tschermak's substitution ( $\text{Fe}^{2+}\text{Si}^{4+} \leftrightarrow 2\text{Fe}^{3+}$ ). **D:** Fe<sup>3+</sup> greenalite, constructed assuming a vacancy substitution in 1/3 of octahedral sites ( $3\text{Fe}^{2+} \leftrightarrow 2\text{Fe}^{3+}\square$ ). **E:** Ferrihydrite from the structural model of Michel et al. (2007).

335

336 2.4. *Ab initio* calculation of reduced partition function ratios for iron in greenalite and ferrihydrite

337 We conducted *ab initio* density functional theory (DFT) calculations to determine the force  
338 constant and reduced partition function ratios for ferrihydrite, and greenalite and related minerals  
339 with a range of Fe valence states. For greenalite, we modeled the Fe<sup>2+</sup> endmember with the  
340 monoclinic cell corresponding to the composition Fe<sub>3</sub>Si<sub>2</sub>O<sub>5</sub>(OH)<sub>4</sub> (Fig. 3A). Following the  
341 observation that Fe<sup>3+</sup> is predominantly accommodated in octahedral sites in greenalite by vacancy  
342 substitution<sup>88</sup>, we modeled a mixed valence greenalite (Fe<sup>3+</sup>/Fe<sub>tot</sub> = 0.4) with a monoclinic cell  
343 with one third of octahedral sites occupied by Fe<sup>3+</sup> (in adjacent sites), compensated by every sixth  
344 site being occupied by a vacancy (adjacent to the Fe<sup>3+</sup> sites) (Fe<sup>2+</sup><sub>3</sub>Fe<sup>3+</sup><sub>2</sub>□Si<sub>4</sub>O<sub>10</sub>(OH)<sub>8</sub>) (Fig. 3B).  
345 We also explored a mixed-valence (Fe<sup>3+</sup>/Fe<sub>tot</sub> = 0.5) cronstedtite-like model wherein octahedral  
346 Fe<sup>3+</sup> was compensated by Fe<sup>3+</sup> substituting for Si<sup>4+</sup> in tetrahedra (Fig. 3C). This ferri-Tschermak's  
347 [Fe<sup>2+</sup>Si<sup>4+</sup> ↔ 2 Fe<sup>3+</sup>] substitution is observed to be the dominant form of Fe<sup>3+</sup> incorporation into  
348 naturally occurring Mg-rich serpentines<sup>89</sup>. This model is less relevant to the origin of IFs but  
349 provides an interesting test of how different modes of Fe<sup>3+</sup> incorporation impact the Fe force  
350 constant and equilibrium isotopic behavior of Fe in serpentines. We modeled an Fe<sup>3+</sup> endmember  
351 for greenalite with a monoclinic structure corresponding to the composition Fe<sub>2</sub>Si<sub>2</sub>O<sub>5</sub>(OH)<sub>4</sub> (Fig.  
352 3D). This Fe<sup>3+</sup> endmember formula for greenalite does not occur naturally, however a very similar  
353 mineral, hisingerite (Fe<sub>2</sub>Si<sub>2</sub>O<sub>5</sub>(OH)<sub>4</sub>·nH<sub>2</sub>O) does occur in nature, associated with low-temperature  
354 alteration of ferroan olivine<sup>90</sup>. In hisingerite, charge balance is also maintained by the substitution  
355 of octahedral site vacancies, with the end point of this compositional vector being  
356 □Fe<sup>3+</sup><sub>2</sub>Si<sub>2</sub>O<sub>5</sub>(OH)<sub>4</sub>·nH<sub>2</sub>O<sup>90</sup>. We modeled the Fe<sup>3+</sup> endmember by applying the vacancy  
357 substitution to every third Fe site (Fig. 3D). The principal difference between this modeled

358 structure and hisingerite is that hisingerite is hydrated, however the structures are similar, and we  
359 might expect that the force constant determined here may be similar to that for hisingerite.

360

361 The ferrihydrite ( $\text{Fe}_5\text{O}_8\text{H}$ ) model was built from the akdalaite hexagonal structure proposed by  
362 Michel et al.<sup>91</sup> where Fe atoms are both tetrahedrally and octahedrally coordinated (Fig. 3E). We  
363 did not attempt to model the multi-component ferrihydrite model of Drits et al.<sup>92</sup> due to its greater  
364 complexity. Most DFT calculations have used the Michel et al.<sup>91</sup> model for the same reason. Sassi  
365 et al.<sup>93</sup> recently investigated the two structural models by DFT and concluded that ferrihydrite may  
366 be a nanocomposite of the two endmember models proposed by Michel et al.<sup>91</sup> and Drits et al.<sup>92</sup>,  
367 with the proportions of each structure depending on particle size, temperature, pH, and water  
368 partial pressure. Sassi et al.<sup>93</sup> also showed that the Michel and Drits models are thermodynamically  
369 equivalent across a wide range of conditions.

370

371 Structural relaxations used the PWscf code<sup>94</sup> (<http://www.quantum-espresso.org>) using the DFT  
372 plus Hubbard  $U$  method (DFT +  $U$ ) and the generalized gradient approximation (GGA) to the  
373 exchange-correlation functional with the PBE parameterization<sup>95</sup>. The ionic cores were described  
374 by ultrasoft pseudopotentials from the Garrity-Bennett-Rabe-Vanderbilt (GBRV) library<sup>96</sup>. After  
375 energy convergence tests, the wave-functions and the charge density were expanded in plane-  
376 waves with 40 and 400 Ry cutoffs, respectively. For the electronic integration, the Brillouin zone  
377 was sampled according to the Monkhorst-Pack scheme<sup>97</sup>, using shifted  $2 \times 2 \times 2$   $k$ -point grids.  
378 Calculations were spin-polarized and magnetic moments were free to relax. The ferrihydrite  
379 magnetic ordering was set to be ferrimagnetic, with the Fe-site spins ordering with alternating  
380 alignment in layers stacked along the  $c$ -direction in the crystallographic unit cell, following the

381 theoretical investigation of Pinney et al.<sup>98</sup>. Greenalite displays antiferromagnetically ordered  
 382 layers<sup>99</sup>. However, since we used a one-layer unit cell, our model imposed a ferromagnetic  
 383 structure by periodic repetition of layers with parallel magnetic alignments. The value of the  
 384 Hubbard  $U$  for Fe sites was determined using a linear response approach in an internally consistent  
 385 manner<sup>100,101</sup>. Details of the practical procedure can be found in Blanchard et al.<sup>73</sup>.

386  
 387 Following the method reviewed in detail by Blanchard et al.<sup>102</sup>, Fe  $\beta$ -factors were calculated from  
 388 their harmonic vibrational frequencies using

$$389 \beta(\alpha, Y) = \left[ \prod_{i=1}^{3N_{\text{at}}} \prod_{\{q\}} \frac{v_{q,i}^* e^{-hv_{q,i}^*/(2kT)}}{v_{q,i} e^{-hv_{q,i}/(kT)}} \frac{1 - e^{-hv_{q,i}/(kT)}}{e^{-hv_{q,i}/(2kT)}} \right]^{1/(N_q N)}, \quad (\text{Eq. 6})$$

390 where  $v_{q,i}$  are the frequencies of the phonon with wavevector  $q$  and branch index  $i = 1, 3N_{\text{at}}$ , and  
 391 where  $N_{\text{at}}$  is the number of atoms in the unit cell.  $v_{q,i}$  and  $v_{q,i}^*$  are the vibrational frequencies in two  
 392 isotopologues.  $N$  is the number of sites for the  $Y$  atom in the unit cell,  $T$  is the temperature,  $h$  is  
 393 the Planck constant and  $k$  is the Boltzmann constant.

**Table 1:** Cell parameters optimized by DFT +  $U$  for modeled greenalite and ferrihydrite compared to experimental data.

	Gr exp*	Fe <sup>2+</sup> Gr	Fe <sup>2.4+</sup> Gr (octahedral vacancy substitution)	Fe <sup>2.5+</sup> Gr (Ferri- Tschermak substitution)	Fe <sup>3+</sup> Gr	Fh exp*	Fh
<b>a</b> (Å)	5.54	5.50	5.45	5.67	5.34	5.95	6.05
<b>b</b> (Å)	9.55	9.53	9.37	9.82	9.28	5.95	6.05
<b>c</b> (Å)	7.44	7.74	7.73	7.43	7.60	9.06	9.40
<b><math>\alpha</math></b> (°)	90.0	89.7	90.0	90.7	90.4	90.0	90.0
<b><math>\beta</math></b> (°)	104.2	103.5	103.4	105.4	104.3	90.0	90.0
<b><math>\gamma</math></b> (°)	90.0	90.1	90.0	90.0	89.8	120.0	120.0

\*Experimental data for greenalite and ferrihydrite were taken from Gruner (1936) and Michel et al. (2007) respectively.

394

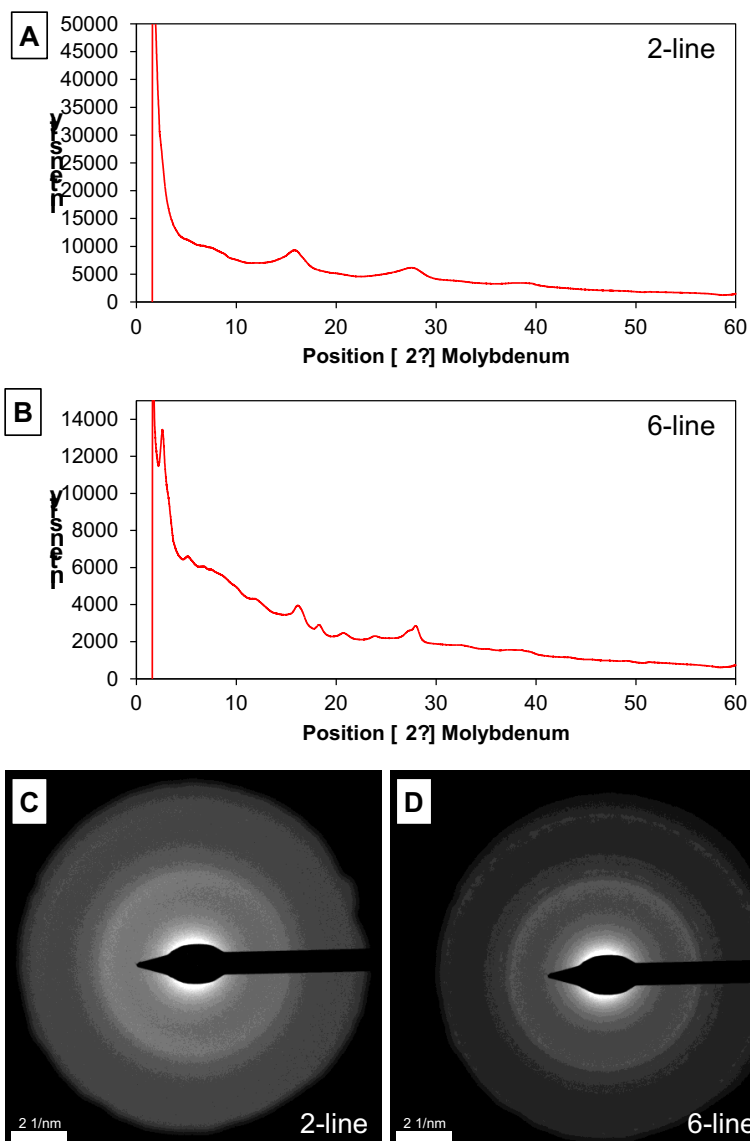


**Fig. 4:** Structural analysis of synthesized ferrihydrite. **A:** XRD analysis of 2-line ferrihydrite. **B:** XRD analysis of 6-line ferrihydrite. **C:** HR-TEM SAED analysis of 2-line ferrihydrite. **D:** HR-TEM SAED analysis of 6-line ferrihydrite. All patterns agree with published values (Janney et al., 2000; Lee and Xu, 2019).

395 Phonon frequencies were calculated within the harmonic approximation using the linear response  
 396 theory<sup>103</sup> as implemented in the PHonon code<sup>94</sup> (<http://www.quantum-espresso.org>). Phonon  
 397 frequencies were computed on a centered  $2 \times 2 \times 2$   $q$ -point grid for ferrihydrite and using one  $q$ -  
 398 point shifted with respect to the center of the Brillouin zone for greenalite. Tests using the

399 computationally less demanding DFT method (without Hubbard  $U$ ) showed that considering only  
400 one shifted  $q$ -point led to a relative uncertainty smaller than 3% on both the  $\beta$  and  $\langle F \rangle$ . The same  
401 linear response calculations provided the average force constant  $\langle F \rangle$  of each Fe crystallographic  
402 site. This quantity corresponds to the harmonic restoring force constants, along the three  
403 orthogonal directions, that tend to pull back the studied atom in its equilibrium position. and can  
404 be calculated from the linear response method. This method was also used for instance in Aarons  
405 et al.<sup>104</sup> and Dauphas et al.<sup>105</sup>. All cell parameters from models are detailed in Table 1, and the  
406 experimental data used to validate the model results for greenalite and ferrihydrite were taken from  
407 Gruner (1936)<sup>106</sup> and Michel et al. (2007)<sup>91</sup> respectively

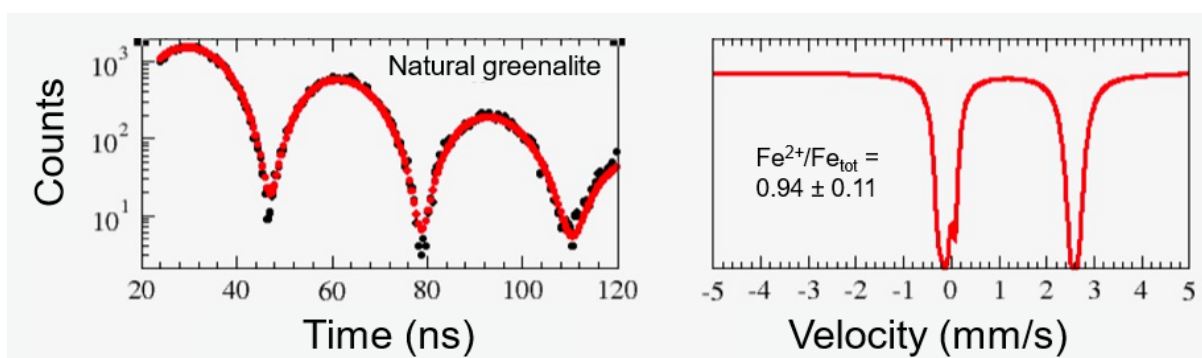


**Figure 5. Left:** Time domain synchrotron Mössbauer spectra (SMS) of natural greenalite standard left column. **Right:** Corresponding simulated energy domain spectra presented in the more familiar Doppler velocity shift units. The isomer shifts are relative to the Fe<sup>3+</sup> component which is set to zero. The CONUSS program<sup>9</sup> was used for data evaluation and simulations. Estimated Fe redox states and associated errors are shown on the right-hand panels. The sample was determined to have  $\text{Fe}^{2+}/\text{Fe}_{\text{tot}} = 0.94 \pm 0.11$ .

408

### 409 3. RESULTS

#### 410 3.1. Mineral characterization results

411 The XRD spectra obtained on the synthesized ferrihydrite samples (Figs. 4A-B) were consistent  
412 with those expected for 2-line and 6-line ferrihydrite, respectively<sup>107</sup>. From HR-TEM analysis, the

413 lattice planes in SAED patterns agreed well with published data for 2-line and 6-line ferrihydrite  
414 (Figs. 4C-D)<sup>79</sup>. Images of 2-line ferrihydrite suggested crystallite sizes of ~2.5 nm, though the  
415 domain divisions were mostly indistinct. Images of 6-line ferrihydrite showed clearer domains of  
416 ~5 nm diameter. Fits to the forward-scattering spectrum for the natural greenalite standard using  
417 the CONUSS software<sup>85</sup> indicated ~94 % Fe<sup>2+</sup> and ~6 % Fe<sup>3+</sup> ( $\text{Fe}^{2+}/\text{Fe}_{\text{tot}} = 0.94 \pm 0.11$ ; Table 2,  
418 Fig. 5). The statistically insignificant quantity of Fe<sup>3+</sup> in this sample allows us to treat it as a ferrous  
419 endmember for NRIXS interpretations.

420

### 421 3.2. NRIXS and DFT + U results

422 The measured and calculated pDOS are provided in a spreadsheet as supplementary online  
423 materials, including the calculated pDOS for Fe in each of the three crystallographic sites in the  
424 modeled ferrihydrite. The polynomial expressions for  $\beta$  are given in Table 2, where we display the  
425 first three terms. The force constants for each mineral are also compiled in Table 2. NRIXS  
426 measurements and *ab initio* calculations yield the Fe pDOS (Fig. 6, Supplementary Material),  $\langle F \rangle$   
427 values (Figs. 7-8, Table 2), and  $\beta$  factors (using Eq. 2; Fig. 9, Table 2) in 2L-, 6L-ferrihydrite and  
428 greenalite. In the simulations, the DFT + *U* approach resulted in a relaxed structure that better fits  
429 experimental constraints on the crystallographic dimensions for Fe<sup>2+</sup> greenalite ( $\text{Fe}_3\text{Si}_2\text{O}_5(\text{OH})_4$ )  
430 than DFT alone, whilst for other minerals DFT + *U* and simpler DFT approaches gave similar  
431 levels of agreement with experiments (Table 1, Fig. 3). We thus report and focus our discussion  
432 of simulations on the DFT + *U* results. DFT based force constants (not reported) were shifted to  
433 lower force constant values by about 40 N/m compared to DFT + *U*. Because interpretations of  
434 natural isotopic variations rely on differences between  $\beta$ -factors between minerals and we do not



435 mix results obtained from different methods, a constant shift in force constant does not affect the  
436 conclusions.

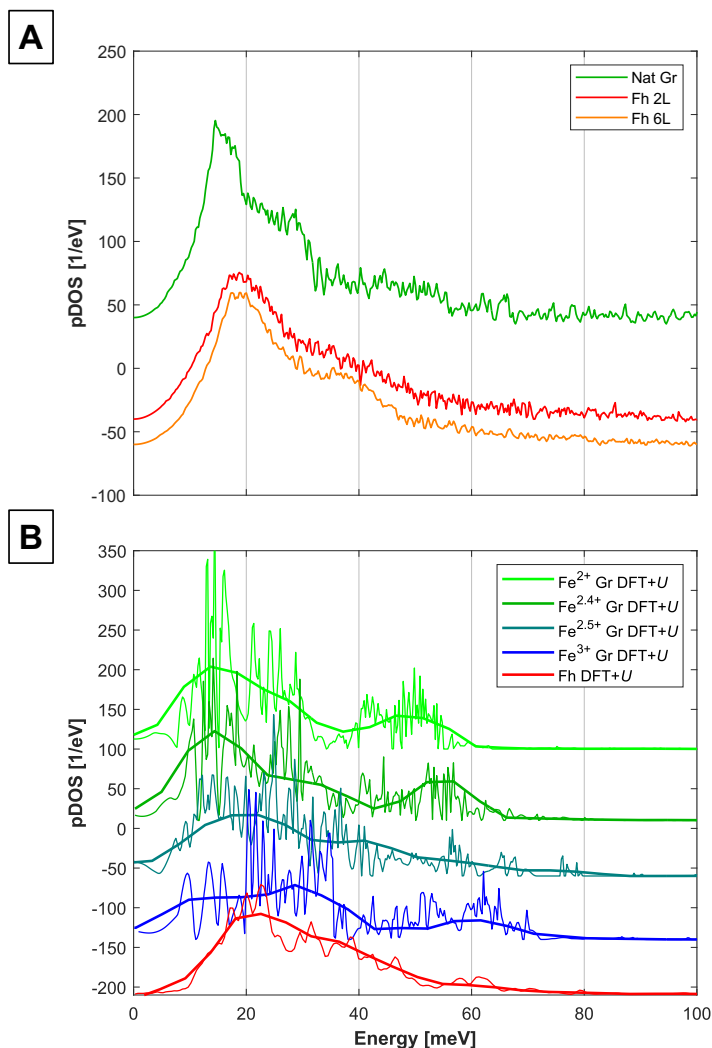


**Figure 6. A:** Average measured partial phonon density of states (pDOS) of iron in natural greenalite (Nat Gr) and laboratory synthesized ferrihydrite (Fh), determined by NRIXS analysis. **B:** Partial phonon density of states (pDOS) of iron in Fe<sup>2+</sup>, Fe<sup>2.4+</sup> (vacancy substituted) Fe<sup>2.5+</sup> (Ferri-Tschermak substituted) and Fe<sup>3+</sup> (vacancy substituted) greenalite (Gr), and ferrihydrite (Fh), determined by DFT+*U* simulations. Raw pDOS and pDOS smoothed for clarity of broad features are shown in lighter and heavier lines, respectively. All data are provided in a spreadsheet as supplementary online materials. pDOS curves are arbitrarily shifted on the vertical axis to improve readability in **A** and **B**, with increasingly oxidized materials shown lower in the vertical order.

437

<b>Table 2.</b> Polynomial fits for $1000\ln\beta = A_1X + A_2X^2 + A_3X^3$ , with $X = 10^6/T^2$ (T in K), and force constants, $\langle F \rangle$ , for Fe in greenalite and ferrihydrite. Error bars show the 95 % confidence interval on NRIXS determinations, and 3% estimated relative uncertainty on $\langle F \rangle$ values determined via DFT + $U$ based on uncertainties in vibrational frequencies.				
	<b>A<sub>1</sub></b>	<b>A<sub>2</sub></b>	<b>A<sub>3</sub></b>	<b><math>\langle F \rangle</math> (N m<sup>-1</sup>)</b>
<b>DFT + <math>U</math></b>				
<b>Fe<sup>2+</sup> Greenalite</b>	$6.12 \times 10^{-1} \pm 1.84 \times 10^{-2}$	$-2.75 \times 10^{-3} \pm 8.25 \times 10^{-5}$	$2.13 \times 10^{-5} \pm 6.39 \times 10^{-7}$	$214 \pm 6$
<b>Fe<sup>2.4+</sup> Greenalite (octahedral vacancy)</b>	$7.04 \times 10^{-1} \pm 2.11 \times 10^{-2}$	$-3.97 \times 10^{-3} \pm 1.19 \times 10^{-4}$	$3.70 \times 10^{-5} \pm 1.11 \times 10^{-6}$	$243 \pm 7$
<b>Fe<sup>2.5+</sup> Greenalite (ferri-Tschermak)</b>	$6.79 \times 10^{-1} \pm 2.04 \times 10^{-2}$	$-4.02 \times 10^{-3} \pm 1.21 \times 10^{-4}$	$4.37 \times 10^{-5} \pm 1.31 \times 10^{-6}$	$238 \pm 7$
<b>Fe<sup>3+</sup> Greenalite</b>	$8.42 \times 10^{-1} \pm 2.53 \times 10^{-2}$	$-5.73 \times 10^{-3} \pm 1.72 \times 10^{-4}$	$5.94 \times 10^{-5} \pm 1.78 \times 10^{-6}$	$295 \pm 9$
<b>Ferrihydrite</b>	$7.08 \times 10^{-1} \pm 2.12 \times 10^{-2}$	$-3.84 \times 10^{-3} \pm 1.15 \times 10^{-4}$	$3.48 \times 10^{-5} \pm 1.04 \times 10^{-6}$	$235 \pm 7$
<b>NRIXS</b>				
<b>Natural Greenalite</b>	$6.32 \times 10^{-1} \pm 8.2 \times 10^{-2}$	$-4.80 \times 10^{-3} \pm 1.79 \times 10^{-3}$	$1.06 \times 10^{-4} \pm 6.52 \times 10^{-5}$	$222 \pm 29$
<b>Ferrihydrite 2L</b>	$7.31 \times 10^{-1} \pm 3.7 \times 10^{-2}$	$-4.71 \times 10^{-3} \pm 6.9 \times 10^{-4}$	$6.96 \times 10^{-5} \pm 2.47 \times 10^{-5}$	$256 \pm 13$
<b>Ferrihydrite 6L</b>	$7.52 \times 10^{-1} \pm 3.7 \times 10^{-2}$	$-5.56 \times 10^{-3} \pm 8.5 \times 10^{-4}$	$1.19 \times 10^{-5} \pm 3.81 \times 10^{-5}$	$263 \pm 13$
<b>Ferrihydrite average</b>	$7.41 \times 10^{-1} \pm 2.6 \times 10^{-2}$	$-5.04 \times 10^{-3} \pm 5.4 \times 10^{-4}$	$8.44 \times 10^{-5} \pm 2.07 \times 10^{-5}$	$260 \pm 9$

438 The pDOSs calculated from NRIXS data (Fig. 6A) lack sharp features seen in DFT +  $U$   
439 calculations. This is not likely due to the finite energy resolution of the monochromator because  
440 SciPhon implements an iterative procedure to deconvolve the energy resolution function from the  
441 measured spectrum<sup>84</sup>. A more plausible explanation is that it is due to the fine-grained or  
442 amorphous nature of the targeted powder samples.

443

444 *3.2.1. Greenalite  $\langle F \rangle$  values and pDOS*

445 The DFT+ $U$  calculations produced  $\langle F \rangle$  values of  $214 \pm 6$ ,  $243 \pm 7$ , and  $295 \pm 9$  N m<sup>-1</sup> for Fe<sup>2+</sup>,  
446 Fe<sup>2.4+</sup>, and Fe<sup>3+</sup> greenalite, and  $238 \pm 7$ , for Fe<sup>2.5+</sup> cronstedtite, respectively (Figs. 7-8, Table 2).  
447 There is a very strong ( $R^2 = 0.9977$ ) negative correlation between Fe<sup>2+</sup>/Fe<sub>tot</sub> and  $\langle F \rangle$  in the  
448 simulated greenalites suggesting that Fe valence state is the sole control on  $\langle F \rangle$  in this mineral  
449 (Fig. 7). Meanwhile, the Fe<sup>2.5+</sup> cronstedtite falls off of this trendline, likely reflecting the different  
450 average bonding environment for Fe in this structure with Fe in both octahedral and tetrahedral  
451 sites (Fig. 3C). For the natural (ferrous) greenalite standard, we calculated  $\langle F \rangle = 222 \pm 29$  N m<sup>-1</sup>  
452 using  $S(E)$  from NRIXS (Figs. 7-8, Table 2).

453

### 454 3.2.2. Ferrihydrite $\langle F \rangle$ values and pDOS

455 The DFT +  $U$  for ferrihydrite (Fe<sub>5</sub>O<sub>8</sub>H) gave a  $\langle F \rangle$  value of  $235 \pm 7$  Nm<sup>-1</sup>. For the NRIXS analysis  
456 of experimentally synthesized ferrihydrite, we present a weighted average  $\langle F \rangle$  value of  $260 \pm 9$  N  
457 m<sup>-1</sup>, as the values for 2-line and 6-line ferrihydrite were identical within error (Figs. 7-8, Table 2).  
458 The pDOS determined for both ferrihydrite structures via NRIXS compared favorably, both in  
459 terms of shape and position of the energy peak, with the pDOS determined from the DFT +  $U$   
460 ferrihydrite model.

461

### 462 3.2.3. Comparison of $\langle F \rangle$ values in greenalite and ferrihydrite

463 Both DFT +  $U$  and NRIXS results showed that Fe<sup>2+</sup>-greenalite has a lower Fe force constant than  
464 ferrihydrite and should thus impart a lighter Fe isotopic composition than ferrihydrite at  
465 equilibrium. DFT +  $U$  results indicate that mixed-valence forms of greenalite and cronstedtite have  
466 Fe force constants similar to ferrihydrite and consequently may have similar Fe isotopic  
467 compositions to ferrihydrite at equilibrium. From DFT +  $U$ , the  $\langle F \rangle$  value of ferrihydrite is 21 N

468  $\text{m}^{-1}$  higher than that of  $\text{Fe}^{2+}$ -greenalite, and identical within error to that of  $\text{Fe}^{2.4+}$  greenalite and  
 469  $\text{Fe}^{2.5+}$  cronstedtite (Fig. 7).

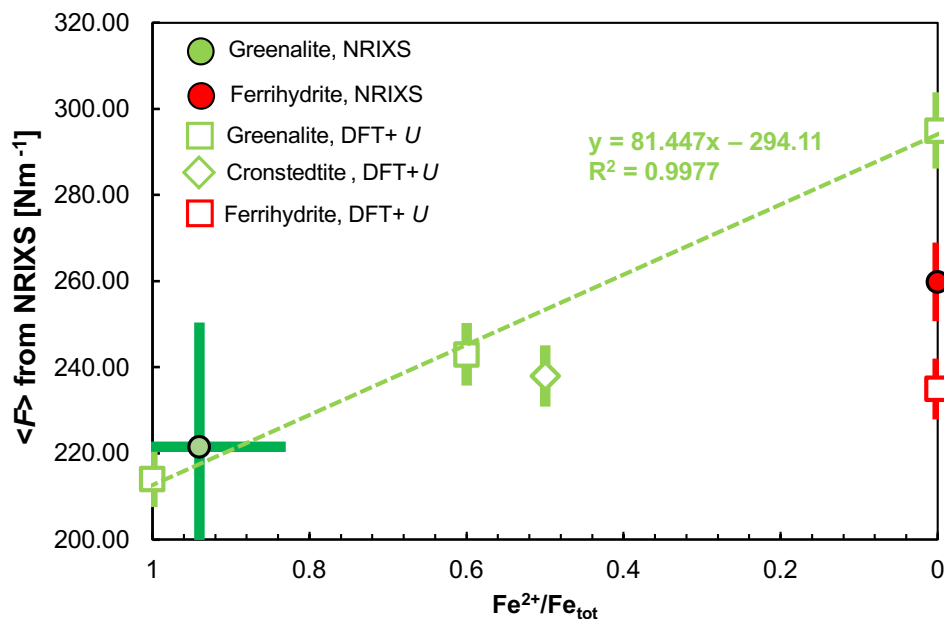


**Figure 7.** Force constant ( $\langle F \rangle$ ) of greenalite and ferrihydrate, vs.  $\text{Fe}^{2+}$  content as a proportion of total Fe ( $\text{Fe}_{\text{tot}}$ ). Filled circles show  $\langle F \rangle$  for the natural greenalite standard (green) and the error weighted average of 2-line and 6-line ferrihydrate (red) from NRIXS analyses. Open squares show  $\langle F \rangle$  for greenalite (green) and ferrihydrate (red) from DFT +  $U$  calculations (right-hand axis). Open green diamond shows  $\langle F \rangle$  for cronstedtite with a ferri-Tschermak substitution. The green dashed line shows the linear correlation between Fe valence state and  $\langle F \rangle$  in modeled greenalites (not including cronstedtite). Error bars show the 95 % confidence interval on NRIXS determinations, and 3% relative uncertainty on  $\langle F \rangle$  values determined via DFT +  $U$ .

470

#### 471 3.2.4. Discrepancy between DFT + $U$ and NRIXS determinations of $\langle F \rangle$

472 The  $\langle F \rangle$  of  $\text{Fe}^{3+}$  in ferrihydrate determined from DFT +  $U$  simulations is  $\sim 25 \text{ N m}^{-1}$  lower than the  
 473 average value determined from NRIXS. This offset is similar to that observed between DFT +  $U$   
 474 calculations and NRIXS determinations of  $\langle F \rangle$  for goethite<sup>62</sup> and larger than the one previously  
 475 observed for hematite<sup>63</sup> (Fig. 8). It should also be noted here that the DFT +  $U$  results for  
 476 ferrihydrate (using Michel<sup>91</sup> model) and goethite<sup>62</sup> have similar Fe force constants that overlap

477 within error, and it is thus expected that the Drits<sup>92</sup> model ferrihydrite, which is more similar to  
478 the Michel model ferrihydrite than it is to goethite, would fall within this range as well. For natural  
479 Fe<sup>2+</sup> greenalite, the  $\langle F \rangle$  determined via NRIXS agreed within the 95% confidence interval with the  
480 calculated based on DFT +  $U$ . All data from this study, along with previous goethite and hematite  
481 data<sup>62,63</sup>, are consistent within error with an average 16 N m<sup>-1</sup> offset to higher values in NRIXS vs.  
482 DFT +  $U$  determinations of  $\langle F \rangle$  (Fig. 8). Due to the offset between *ab initio* and NRIXS  
483 determinations of  $\langle F \rangle$ , below we only consider Fe isotopic fractionations between ferrihydrite and  
484 greenalite determined via a single method (NRIXS or DFT +  $U$ ) rather than mixing outputs from  
485 different approaches.

486

### 487 3.2.5. Equilibrium iron isotopic fractionations between ferrihydrite and greenalite

488 We describe Fe isotopic fractionations in terms of  $1000\ln\alpha$  values (where we consider the <sup>56</sup>Fe/<sup>54</sup>Fe  
489 ratio), using  $\beta$  factors calculated from the three-term polynomial expansion at 22 °C (Table 2), to  
490 enable comparison to previous experimental work, and present fractionations on the familiar  $\delta^{56}\text{Fe}$   
491 scale. We define the following abbreviations for the phases used in calculating  $\alpha$  values: Fh –  
492 ferrihydrite; Gr2+ – reduced or ferrous greenalite, represented by the modeled Fe<sup>2+</sup> endmember  
493 and the natural ferrous greenalite standard, in DFT +  $U$  and NRIXS determinations, respectively;  
494 Gr2.4+ – mixed valence greenalite, represented by the modeled Fe<sup>2.4+</sup> structure in DFT +  $U$ ; and  
495 Gr3+ – oxidized greenalite, represented by the modeled Fe<sup>3+</sup> endmember in DFT +  $U$ . We focus  
496 our discussion and interpretations on the greenalites with all Fe in octahedral sites and Fe<sup>3+</sup>  
497 accompanied by vacancy substitution, because Mössbauer studies indicate that this is the site  
498 where Fe<sup>3+</sup> substitution takes place in naturally occurring greenalite<sup>88</sup>. Results for the cronstedtite-

499 type model are displayed in figures but are not discussed at length below in reference to the Fe  
 500 isotopic record of IFs.

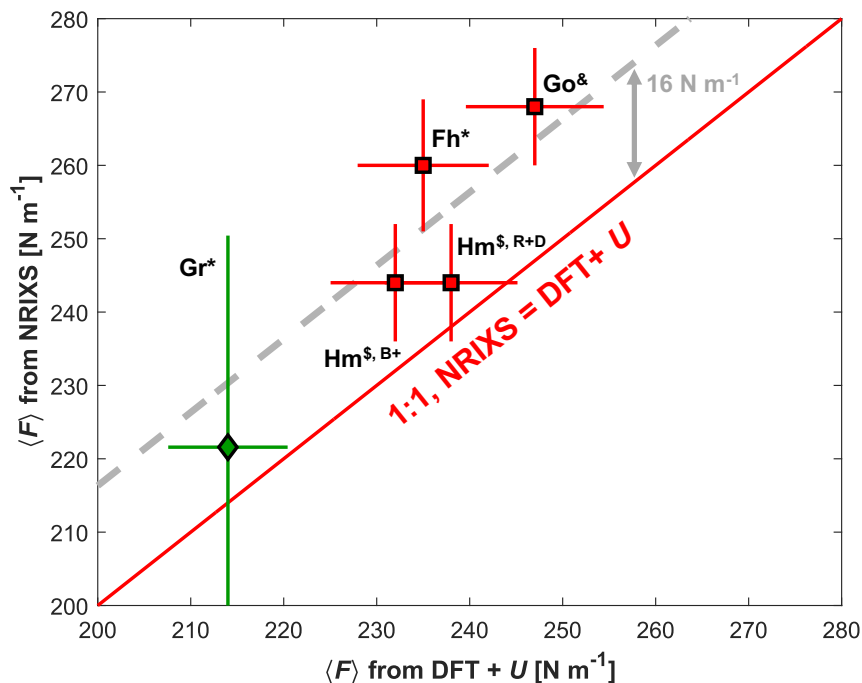


**Figure 8.** Intercomparison of force constants  $\langle F \rangle$  data from NRIXS and *ab initio* DFT+U simulations for natural greenalite (Gr), ferrihydrite (Fh), goethite (Go), and hematite (Hm), from this study and literature. Greenalite is displayed as a green diamond, and ferric (oxyhydr)oxides are displayed as red squares. The black dotted line is a slope 1:1 line where data would fall if there was perfect agreement between the two techniques. The grey dashed line shows a slope 1 line that minimizes error-weighted deviations of the datapoints and indicates a  $\sim 16 \text{ N m}^{-1}$  offset to higher values in NRIXS determinations versus DFT + U determinations of  $\langle F \rangle$  that is similar to that observed in previous studies of ferric (oxyhydr)oxide minerals (Blanchard et al., 2015; Dauphas et al., 2012). Error bars show the 95 % confidence interval on NRIXS determinations, and 3% relative uncertainty on  $\langle F \rangle$  values determined via DFT + U. Superscripts: \* NRIXS and DFT+U data from this study; & NRIXS and DFT+U data from Blanchard et al. (2015); § NRIXS data from Dauphas et al. (2012); B+ DFT+U data from Blanchard et al. (2009); R+D DFT data from Rustad and Dixon (2009).

501  
 502 From DFT + U,  $1000 \ln \alpha_{\text{Fh-Gr}^{2+}} = +0.98 \pm 0.31 \text{ ‰}$  and from NRIXS,  $1000 \ln \alpha_{\text{Fh-Gr}^{2+}} = 1.19 \pm 1.34 \text{ ‰}$   
 503 (Fig. 9). Most of the uncertainty in this case results from the less precise NRIXS-derived force  
 504 constant for natural greenalite. These results agree very well in indicating a  $\sim 1 \text{ ‰}$  equilibrium Fe

505 isotopic fractionation between ferrihydrite and ferrous greenalite, favoring higher  $^{56}\text{Fe}/^{54}\text{Fe}$  in  
506 ferrihydrite. From DFT +  $U$ ,  $1000\ln\alpha_{\text{Fh-Gr}2.4+} = +0.06 \pm 0.32 \text{ ‰}$  (Fig. 9). These data suggest that  
507 the equilibrium fractionation between mixed valence greenalite compositions and ferrihydrite  
508 could be small compared to many low temperature fractionations typically observed between  
509 species with different Fe redox states. Last, from DFT+ $U$ ,  $1000\ln\alpha_{\text{Fh-Gr}3+} = -1.32 \pm 0.36 \text{ ‰}$  (Fig.  
510 9). This result indicates that an  $\text{Fe}^{3+}$  endmember of greenalite should be significantly isotopically  
511 heavier than coexisting ferrihydrite and other HFOs, which might also predict that naturally  
512 occurring hisingerite, which is structurally similar to our modeled endmember, may take on a very  
513 heavy Fe isotopic composition during its formation during serpentinization of ferroan peridotites<sup>90</sup>.  
514

## 515 4. DISCUSSION

### 516 4.1. Predicting equilibrium iron isotopic fractionations during greenalite precipitation

517 Fluid-mineral equilibration experiments have consistently resulted in  $1000\ln\alpha_{\text{Ferrihydrite-Fe(II)}_{\text{aq}}}$ ,  
518  $1000\ln\alpha_{\text{Hematite-Fe(II)}_{\text{aq}}}$ , and  $1000\ln\alpha_{\text{Fe(III)-Fe(II)}_{\text{aq}}}$  values on the order of  $+3.0 - 3.2 \text{ ‰}$  for  $\delta^{56}\text{Fe}$ <sup>58,59,66</sup>  
519 at around 22 °C (Fig 10). These results indicate that i) the fractionation during ferric oxide  
520 equilibration with an  $\text{Fe}^{2+}$  solution is dominated by the equilibrium fractionation between  $\text{Fe(II)}_{\text{aq}}$   
521 and  $\text{Fe(III)}_{\text{aq}}$ <sup>59</sup>, and ii) the equilibrium fractionation between ferric oxides and aqueous  $\text{Fe(III)}$  is  
522 small<sup>58</sup>. An outlier among this class of experiments is the finding of a  $\sim 1 \text{ ‰}$  fractionation between  
523  $\text{Fe(II)}$  and goethite<sup>55</sup>. However, similar force constants were found for ferrihydrite and goethite in  
524 this study and that of Blanchard et al.<sup>62</sup>, with goethite having a slightly ( $\sim 10 \text{ Nm}^{-1}$ ) higher value of  
525  $\langle F \rangle$  in both DFT+ $U$  and NRIXS datasets, which draws the small  $1000\ln\alpha_{\text{Goethite-Fe(II)}_{\text{aq}}}$   
526 determinations into question. Surface exchange effects were a complicating factor in interpreting

527 the equilibration experiments of Beard et al.<sup>55</sup> and these might have impacted the net fractionation  
 528 during goethite formation while obscuring the equilibrium value of  $1000\ln\alpha_{\text{Goethite-Fe(II)aq}}$ .  
 529

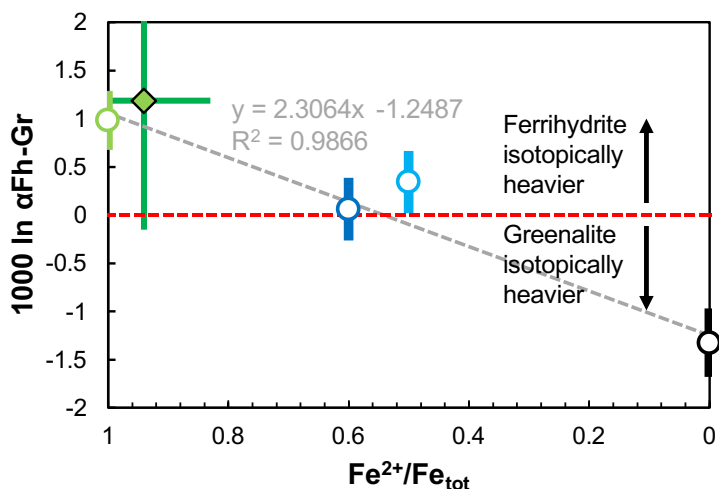


**Figure 9.** Equilibrium Fe isotopic fractionations between ferrihydrite and greenalite materials determined in this study, expressed as  $1000 \ln \alpha_{\text{Fh-Gr}}$  for the  $^{56}\text{Fe}/^{54}\text{Fe}$  ratio, where a positive value indicates relative enrichment of heavy Fe isotopes in ferrihydrite. Different symbols show  $1000 \ln \alpha_{\text{Fh-Gr}}$  at 22 °C for different greenalite materials and analytical techniques as follows: natural greenalite standard (NRIXS) –filled green diamond; ferrous greenalite via DFT + U – open pale green circle;  $\text{Fe}^{2.4+}$  greenalite via DFT + U – open dark blue circle;  $\text{Fe}^{2.5+}$  cronstedtite via DFT + U – open pale blue circle;  $\text{Fe}^{3+}$  greenalite via DFT + U – open black circle. The grey dashed line shows the linear correlation between Fe valence state and  $1000 \ln \alpha_{\text{Fh-Gr}}$  in modeled greenalites (not including the  $\text{Fe}^{2.5+}$  cronstedtite). Error bars show the 95 % confidence interval on NRIXS determinations, and 3% relative uncertainty on  $\langle F \rangle$  values determined via DFT + U.

530 We take  $1000\ln\alpha_{\text{Fh-Fe(II)aq}} = +3.0 \text{ ‰}$  as a representative value for the equilibrium fractionation  
 531 between ferrihydrite and aqueous Fe(II) for anchoring to ferrihydrite-mineral pairs. Equilibrium  
 532 Fe isotopic fractionations between greenalite and aqueous Fe(II) can then be calculated as  
 533  $1000\ln\alpha_{\text{Fh-Fe(II)aq}} - 1000\ln\alpha_{\text{Fh-Greenalite}}$ . For ferrous greenalite, we find  $1000\ln\alpha_{\text{Gr}^{2+}\text{-Fe(II)aq}} = +2.02 \pm$   
 534  $0.31 \text{ ‰}$  (DFT + U) and  $+1.81 \pm 1.34 \text{ ‰}$  (NRIXS) (Fig. 10). For mixed valence greenalite, we find  
 535  $1000\ln\alpha_{\text{Gr}^{2.4+}\text{-Fe(II)aq}} = +2.94 \pm 0.32 \text{ ‰}$  (DFT+U;  $\text{Fe}^{2+}/\text{Fe}_{\text{tot}} = 0.40$ ) (Fig. 10). For ferric  
 536 greenalite/hisingerite we find  $1000\ln\alpha_{\text{Gr}^{3+}\text{-Fe(II)aq}} = +4.3 \pm 0.36 \text{ ‰}$  (DFT + U) (Fig. 10).

537



538 Experimental studies to constrain the Fe isotopic fractionation during unidirectional Fe(II)<sub>aq</sub>  
539 oxidation and HFO precipitation via various oxidation mechanisms produce much smaller Fe  
540 isotopic fractionations between ferrous iron solutions and ferric precipitates, resulting in values of  
541  $1000\ln\alpha_{\text{HFO-Fe(II)aq}} = 1.5 \text{ ‰}$  (anoxygenic photosynthesis)<sup>57</sup>,  $1.2 \text{ ‰}$  (UV photooxidation)<sup>20</sup>, and  $1.0 \text{ ‰}$   
542 (air/O<sub>2</sub>)<sup>56</sup> (Fig. 10). The reason for these smaller fractionations compared to fluid-mineral  
543 equilibration experiments is likely that during unidirectional Fe<sup>2+</sup> oxidation and HFO precipitation,  
544 full equilibrium between the precipitate and fluid pools is not reached; even though the results of  
545 at least some of these experiments follow the high-temperature limit equilibrium mass  
546 fractionation law<sup>20</sup>. Anchoring greenalite-ferrihydrate mineral pairs to these smaller  $1000\ln\alpha_{\text{HFO-}}$   
547  $\text{Fe(II)aq}$  values for unidirectional oxidation and precipitation would result in considerably smaller  
548 fractionations for greenalite precipitation. For example we would find  $1000\ln\alpha_{\text{Gr2+-Fe(II)aq}} \sim -0.2$  to  
549  $+0.5 \text{ ‰}$ ,  $1000\ln\alpha_{\text{Gr2.4+-Fe(II)aq}} \sim +0.9$  to  $+1.4 \text{ ‰}$  and  $1000\ln\alpha_{\text{Gr3+-Fe(II)aq}} \sim +2.3$  to  $+2.8 \text{ ‰}$  (Fig. 10),  
550 depending on the specific experiment used for anchoring.

551

#### 552 *4.2. Implications for the origins of Archean iron formations*

553 The fractionations calculated from DFT + *U* and NRIXS measurements can be used to address the  
554 Fe isotopic imprint of potential primary greenalite precipitates. We find that equilibrium Fe  
555 isotopic fractionation between a representative HFO precursor for IFs and ferrous greenalite is on  
556 the order of 1–1.2 ‰ for <sup>56</sup>Fe/<sup>54</sup>Fe at 22°C, with ferrihydrate being relatively enriched in <sup>56</sup>Fe. This  
557 result is consistent between DFT+*U* and NRIXS determinations.

558

559 Depending on whether ferrihydrate-greenalite fractionation is anchored to ‘exchange/equilibration’  
560 or ‘unidirectional/precipitation’-style experiments, we can infer fractionations accompanying the

561 precipitation of ferrous greenalite that range from a ~2 ‰ enrichment in  $\delta^{56}\text{Fe}$  relative to the marine  
 562 reservoir to a slightly negative or no fractionation, respectively (Fig. 10). The latter result would

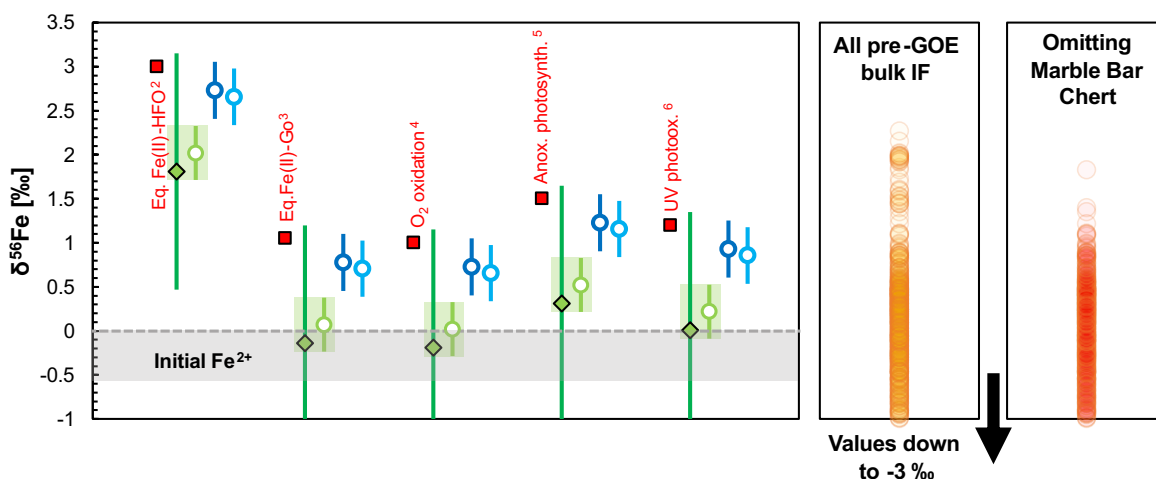


**Figure 10.** Left: Range of possible initial Fe isotopic fractionations during greenalite precipitation determined by anchoring greenalite-ferrihydrite mineral pairs to published fractionations between aqueous Fe(II) at  $\delta^{56}\text{Fe} = 0$  ‰ and hydrous ferric oxide (HFO) determined in different experimental studies (red squares). Symbols showing the fractionation in the greenalite-ferrihydrite mineral pair at 22 °C are the same as those in Fig. 9. Error bars show the 95 % confidence interval on NRIXS determinations, and 3% relative uncertainty on  $\langle F \rangle$  values determined via DFT +  $U$ . Green shaded boxes show the range of fractionations for  $\text{Fe}^{2+}$  greenalite allowed within the error range of both techniques. Superscripts: <sup>1</sup>Heard and Dauphas (2020); <sup>2</sup>Wu et al. (2011); <sup>3</sup>Beard et al. (2010); <sup>4</sup>Bullen et al. (2001); <sup>5</sup>Croal et al. (2004); <sup>6</sup>Nie et al. (2017). Right: Range of  $\delta^{56}\text{Fe}$  observed in pre-GOE IFs for comparison to greenalite fractionations, compiled by Heard and Dauphas (2020). Compilations are shown with (orange, left) and without (red, right) the Marble Bar Chert, which contains the highest  $\delta^{56}\text{Fe}$  values in this record but which may not record primary depositional signatures due to extensive alteration (Rasmussen et al., 2014; Rasmussen and Muhling 2022).

563 immediately rule out a pure ferrous greenalite precursor for IFs (Fig. 10). However, it is not clear  
 564 that anchoring to unidirectional ferrihydrite precipitation experiments is an appropriate assumption  
 565 when calculating the pure equilibrium fractionation involved in greenalite precipitation. Therefore,  
 566 below we expand upon the discussion of fractionations anchored to the +3.0 ‰  
 567 exchange/equilibrium class of experiments and the implications of the largest possible equilibrium  
 568 fractionations that may be associated with  $\text{Fe}^{2+}$  greenalite.

569

570 Our results show that the maximum possible value for  $1000\ln\alpha_{\text{Gr}^{2+}\text{-Fe(II)}_{\text{aq}}}$  is  $+2.02 \pm 0.31 \text{ ‰}$  (DFT  
571  $+ U$ ) or  $+1.81 \pm 1.34 \text{ ‰}$  (NRIXS) (Fig. 10), with the largest value allowable within the error bar  
572 of both techniques being  $+2.3 \text{ ‰}$  (Fig. 10). If a hydrothermal  $\text{Fe}^{2+}$  source to the Archean oceans  
573 had  $\delta^{56}\text{Fe} = 0$ , towards the higher end of values for  $\text{Fe}^{2+}$  inputs to the modern oceans<sup>108,109</sup>, IFs  
574 with  $\delta^{56}\text{Fe}$  values as high as  $2.3 \text{ ‰}$  could therefore be explainable by low degrees of partial  $\text{Fe}^{2+}$   
575 greenalite precipitation at equilibrium. Kinetic isotope effects associated with oversaturation of a  
576 greenalite precursor mineral in solution would potentially decrease this positive fractionation, and  
577 further experiments will need to address this, as discussed in Section 5.

578

579 We compare these inferred fractionations to the pre-GOE bulk rock  $\delta^{56}\text{Fe}$  record of IFs, which  
580 should ideally be unaffected by closed-system inter-mineral fractionation and may represent  
581 primary Fe depositional fluxes. As shown in Figure 10, the inferred value for  $1000\ln\alpha_{\text{Gr}^{2+}\text{-Fe(II)}_{\text{aq}}}$   
582 can account for the Fe isotopic composition of all pre-GOE bulk IF material except the 3.4 Ga  
583 Marble Bar Chert, which has  $\delta^{56}\text{Fe}$  values as high as  $2.6 \text{ ‰}$ . At face value, the inability of  $\text{Fe}^{2+}$   
584 greenalite to reproduce the  $\delta^{56}\text{Fe}$  of such an ancient example of IF material is significant, because  
585 a larger fractionation would require an  $\text{Fe}^{3+}$ -bearing precipitate and necessitate the occurrence of  
586 marine  $\text{Fe}^{2+}$  oxidation since at least 3.4 Ga.

587

588 The Marble Bar Chert does, however, reach considerably higher  $\delta^{56}\text{Fe}$  values than other pre-GOE  
589 bulk IFs, which, outside of a single outlying value, are  $< 1.7 \text{ ‰}$  (Fig. 10). We cannot definitively  
590 determine if the high  $\delta^{56}\text{Fe}$  values of the Marble Bar Chert reflect atypical depositional processes  
591 (for the Archean) or secondary alteration processes that enriched the bulk rock in heavy Fe isotopes

592 relative to the initial precipitate. Microscale petrographic studies of these rocks have revealed that  
593 fine grained hematite originally thought to be primary<sup>61,110</sup>, may instead be an alteration product  
594 of primary greenalite<sup>41,43</sup>. Oxidative alteration would not be expected to reset bulk Fe isotopic  
595 compositions in an IF, given the decreased fluid mobility of Fe<sup>3+</sup> relative to Fe<sup>2+</sup>. A previous study  
596 showed indeed that primary signatures should be retained in bulk  $\delta^{56}\text{Fe}$  values through high grade  
597 metamorphism even without net oxidation<sup>49</sup>. One possible reason why the Marble Bar Chert has  
598 uniquely high  $\delta^{56}\text{Fe}$  relative to other Archean IFs may be its low Fe content ( $[\text{Fe}_2\text{O}_3] < 10 \text{ wt } \%$ )  
599 that strictly characterizes it as a jaspilite. With lower Fe contents, they may have been less strongly  
600 rock-buffered during fluid flow and more susceptible to isotopic overprinting. This low Fe content  
601 alone suggests the Marble Bar Chert is unrepresentative of the general pre-GOE IF record we aim  
602 to compare to isotopic systematics of greenalite. We cannot conclusively rule out the elevated  
603  $\delta^{56}\text{Fe}$  of the Marble Bar Chert as evidence for non-zero levels of Fe<sup>2+</sup> oxidation as early as 3.4 Ga,  
604 but context suggests that this single formation should not be given too much weight in  
605 understanding the early marine Fe cycle.

606

607 It is apparent from the results of this study that Fe isotope systematics alone cannot provide a  
608 constraint on the primary mineralogy of IFs; however, reconciling our data with the rock record  
609 suggests that partial Fe<sup>2+</sup> oxidation is more consistent with the Fe isotopic record and  
610 measurements of early-preserved IF greenalite than pure ferrous greenalite. The DFT + *U*  
611 simulations indicate that greenalite with an average Fe valence state of 2.4+ should impart  
612 essentially identical equilibrium Fe isotopic systematics to ferrihydrite. This valence state is  
613 intriguing because IFs themselves have an average Fe valence state of 2.4<sup>+16</sup>. However,  
614 synchrotron-based analyses of well-preserved pre-GOE IFs suggest that greenalite typically has

615 lower  $\text{Fe}^{3+}$  contents ( $\text{Fe}^{3+}/\text{Fe}_{\text{tot}} \approx 0.1-0.2$ )<sup>39</sup>. Using the relationship between Fe valence state and  
616  $1000\ln\alpha_{\text{Fh-Gr}}$  from our DFT +  $U$  simulations (Fig. 9), we can predict that greenalites with the  
617 recorded range of  $\text{Fe}^{3+}$  contents would form 0.6-0.8 ‰ per mil lighter than ferrihydrite, allowing  
618  $1000\ln\alpha_{\text{Gr-Fe(II)aq}}$  values up to 2.2-2.4 ‰ that account for the entire pre-GOE IF record save for a  
619 few values in the anomalous Marble Bar Chert<sup>61</sup>. Therefore, it is possible that a relatively low- $\text{Fe}^{3+}$   
620 greenalite precursor for pre-GOE IFs may be reconciled with the  $\delta^{56}\text{Fe}$  record even if the most  
621 extreme outlier values are indeed primary depositional signatures.

622

## 623 5. FUTURE DIRECTIONS

624 The uncertainty in predicted greenalite- $\text{Fe(II)}_{(\text{aq})}$  Fe isotopic fractionations, stemming  
625 predominantly from uncertainty in which HFO- $\text{Fe(II)}_{(\text{aq})}$  fractionation factors to anchor to,  
626 underlines the importance of future experimental works to determine the Fe isotopic fractionation  
627 during unidirectional greenalite precipitation from ferrous solutions. Unidirectional greenalite (or  
628 greenalite precursor mineral) precipitation experiments should provide a more refined picture of  
629 Fe isotopic fractionation associated with natural greenalite formation. In particular, experiments  
630 should be conducted with solutions containing both  $\text{Fe}^{2+}$  and  $\text{Mn}^{2+}$ . By coupling  $\delta^{56}\text{Fe}$   
631 measurements with measurements of Mn/Fe in co-sampled solutions and greenalite precursor  
632 precipitates, the chemical evolution of solutions and precipitates could be compared to the well-  
633 established negative correlation seen in  $\ln(\text{Mn}/\text{Fe})$  vs.  $\delta^{56}\text{Fe}$  plots of IFs of all ages<sup>111-115</sup>. This  
634 negative correlation is well-explained by preferential incorporation of Fe into IF precipitates  
635 relative to Mn, because the latter requires higher redox potentials to be oxidized to insoluble  $\text{Mn}^{4+}$   
636 hydroxides<sup>113</sup>. Meanwhile,  $\text{Fe}^{2+}$  and  $\text{Mn}^{2+}$  have very similar geochemical behaviors, so the degree  
637 of incorporation of Mn in  $\text{Fe}^{2+}$ -greenalite and mixed valence greenalite precursor material will

638 offer a useful second variable to disentangle the surprisingly similar  $\delta^{56}\text{Fe}$  systematics of HFOs  
639 and  $\text{Fe}^{3+}$ -bearing greenalite.

640

641 Lastly, our finding that the Fe isotope record could be consistent with a role for greenalite rather  
642 than HFOs as a dominant IF precursor has implications for understanding nutrient availability in  
643 the oceans in deep time, particularly prior to the GOE<sup>33–38</sup>. If a dominant HFO precursor for IF is  
644 not a necessity for ancient ocean chemistry models, it may not be appropriate to quantitatively  
645 reconstruct seawater nutrient concentrations using calibrations to HFO adsorption experiments. It  
646 is thus vital that future experimental studies into the precipitation of greenalite precursor material  
647 should include an exploration of the adsorption and coprecipitation of P, Ni, and other nutrient  
648 elements of interest onto these phases in seawater solutions. Having a more complete  
649 understanding of the range of dissolved [P] levels in the Archean oceans, in particular, may be  
650 vital for assessing the role that nutrient limitation and global rates of photosynthetic primary  
651 productivity played in the eventual rise of atmospheric  $\text{O}_2$ <sup>37,116–118</sup>.

652

## 653 **6. CONCLUSIONS**

654 Assumptions about the primary mineralogy of IFs and iron-rich cherts deposited before the GOE  
655 underpin many aspects of early ocean chemical models. The canonical assumption that HFOs like  
656 ferrihydrite were the dominant precursor minerals in marine chemical sediments informs a view  
657 of the Archean defined by shallow oceans supporting the oxidation of dissolved  $\text{Fe}^{2+}$ , possibly as  
658 a direct or indirect effect of bacterial photosynthesis. The HFO model is also the foundation for  
659 several nutrient reconstructions for the early oceans, which are then interpreted in the context of  
660 biological drivers of changes in ocean and atmospheric oxygenation. An alternative model for pre-

661 GOE IFs and related sediments, informed by detailed petrography, posits that dominantly ferrous  
662 authigenic silicates like greenalite were the primary IF precursor mineral. This model was not  
663 testable with widely available Fe isotopic data for IFs because of a lack of constraints on the Fe  
664 isotopic systematics of greenalite.

665  
666 Here, we determined the Fe force constant ( $\langle F \rangle$ ) and Fe isotope  $\beta$  factors (which determine  
667 equilibrium Fe isotopic fractionation between phases) for greenalite and ferrihydrite, using  
668 DFT+*U ab initio* calculations and NRIXS analysis of natural and laboratory synthesized minerals.  
669 Our results indicate that  $1000\ln\alpha_{\text{Fh-Gr}^{2+}} = +0.98 \pm 0.31 \text{ ‰}$  (DFT + *U*) and  $1.19 \pm 1.34 \text{ ‰}$  (NRIXS),  
670  $1000\ln\alpha_{\text{Fh-Gr}^{2.4+}} = +0.06 \pm 0.32 \text{ ‰}$  (DFT + *U*), and  $1000\ln\alpha_{\text{Fh-GrOx}} = -1.32 \pm 0.36 \text{ ‰}$  (DFT + *U*),  
671 where the modeled oxidized greenalite endmember may provide an estimate of the Fe isotopic  
672 systematics for the naturally-occurring mineral hisingerite.

673  
674 By anchoring these results for fractionations in the greenalite-ferrihydrite mineral pair to published  
675 experimental data on the fractionation of  $\delta^{56}\text{Fe}$  between HFOs and dissolved  $\text{Fe}^{2+}$ , we find that  
676 ferrous greenalite should, at equilibrium, precipitate with  $\delta^{56}\text{Fe}$  fractionated either  $\sim +2 \text{ ‰}$ , or  
677 between  $-0.2$  and  $+0.5 \text{ ‰}$ , relative to dissolved  $\text{Fe}^{2+}$ , depending on if calculated fractionations  
678 were tied to HFO- $\text{Fe(II)}_{\text{aq}}$  equilibration experiments or unidirectional  $\text{Fe(II)}_{\text{aq}}$  oxidation and HFO  
679 precipitation experiments, respectively.

680  
681 This dataset shows that a pathway to reconcile a greenalite-dominated IF depositional flux with  
682 the pre-GOE  $\delta^{56}\text{Fe}$  IF record does exist, provided that either the most uniquely isotopically  
683 enriched pre-GOE IF material does not retain a representative primary depositional signal; or if

684 precipitated greenalite had at least a few tens of %  $\text{Fe}^{3+}$  content due to  $\text{Fe}^{2+}$  oxidation process in  
685 the early oceans. The second of these results ties to the finding of this study that mixed-valence  
686 greenalite should form with similar Fe isotopic compositions to ferrihydrite and is also consistent  
687 with synchrotron-based determinations of low tens of %  $\text{Fe}^{3+}$  in IF greenalite. Because some form  
688 of the greenalite hypothesis appears to be a viable alternative to the HFO model to explain the Fe  
689 isotopic record of IFs, quantitative reconstructions of nutrient elements concentrations like [P] and  
690 [Ni] in the pre-GOE oceans based on HFO adsorption experiments should be viewed with caution.  
691 Comparable experiments featuring authigenic silicate phases like greenalite should be carried out,  
692 along with a variety of further experimental studies on the geochemical and isotopic systematics  
693 of these phases.

694

#### 695 **ACKNOWLEDGEMENTS**

696 Work at the University of Chicago was funded by NASA grants 80NSSC17K0744 to ND and  
697 AWH (Habitable Worlds), 359NNX17AE86G (LARS), NNX17AE87G and 80NSSC20K0821  
698 (Emerging Worlds), 80NSSC20K1409 (Habitable Worlds) to ND, 80NSSC18K1060 (Exobiology)  
699 to JEJ, NSF grant EAR-2001098 (CSEDI) to ND, and a DOE grant to ND. AWH acknowledges  
700 support from an Eckhardt Scholarship from the University of Chicago, a Crosby Postdoctoral  
701 Fellowship from Woods Hole Oceanographic Institution, and an Agouron Institute postdoctoral  
702 fellowship in geobiology. DFT calculations were performed using HPC resources from CALMIP  
703 (Grant 2021-P1037). This research used resources of the Advanced Photon Source, a U.S.  
704 Department of Energy (DOE) Office of Science user facility at Argonne National Laboratory and  
705 is based on research supported by the U.S. DOE Office of Science-Basic Energy Sciences, under



706 Contract No. DE-AC02-06CH11357. Discussions with Andrey Bekker and Chad Ostrander were  
707 appreciated.

708

### 709 **Supplementary Information**

- 710 • Details of laboratory synthesis, characterization, and NRIXS analysis of a hydrous silicate  
711 material intended to be a greenalite precursor phase.
- 712 • Tables containing: full NRIXS analysis results in the form of SciPhon outputs (Table S1);  
713  $\langle F \rangle$  values and polynomial fits to  $1000 \ln \beta = A_1 X + A_2 X^2 + A_3 X^3$  for experimentally  
714 synthesized material analyzed via NRIXS (Table S2) ; and atomic positions for all mineral  
715 structures modeled in DFT +  $U$  simulations (Table S3).

716

717

### 718 **REFERENCES**

- 719 (1) Bekker, A.; Holland, H. D.; Wang, P.-L.; Rumble lii, D.; Stein, H. J.; Hannah, J. L.; Coetzee, L. L.;  
720 Beukes, N. J. Dating the Rise of Atmospheric Oxygen. *Nature* **2004**, *427* (6970), 117–120.  
721 <https://doi.org/10.1038/nature02260>.
- 722 (2) Gumsley, A. P.; Chamberlain, K. R.; Bleeker, W.; Söderlund, U.; Kock, M. O. de; Larsson, E. R.;  
723 Bekker, A. Timing and Tempo of the Great Oxidation Event. *Proc. Natl. Acad. Sci.* **2017**, *114* (8),  
724 1811–1816. <https://doi.org/10.1073/pnas.1608824114>.
- 725 (3) Poulton, S. W.; Bekker, A.; Cumming, V. M.; Zerkle, A. L.; Canfield, D. E.; Johnston, D. T. A 200-  
726 Million-Year Delay in Permanent Atmospheric Oxygenation. *Nature* **2021**, 1–5.  
727 <https://doi.org/10.1038/s41586-021-03393-7>.
- 728 (4) Poulton, S. W.; Canfield, D. E. Ferruginous Conditions: A Dominant Feature of the Ocean through  
729 Earth’s History. *Elements* **2011**, *7* (2), 107–112. <https://doi.org/10.2113/gselements.7.2.107>.
- 730 (5) Derry, L. A.; Jacobsen, S. B. The Chemical Evolution of Precambrian Seawater: Evidence from REEs  
731 in Banded Iron Formations. *Geochim. Cosmochim. Acta* **1990**, *54* (11), 2965–2977.  
732 [https://doi.org/10.1016/0016-7037\(90\)90114-Z](https://doi.org/10.1016/0016-7037(90)90114-Z).
- 733 (6) Holland, H. D. The Oceans; A Possible Source of Iron in Iron-Formations. *Econ. Geol.* **1973**, *68* (7),  
734 1169–1172. <https://doi.org/10.2113/gsecongeo.68.7.1169>.
- 735 (7) Isley, A. E. Hydrothermal Plumes and the Delivery of Iron to Banded Iron Formation. *J. Geol.* **1995**,  
736 *103* (2), 169–185.
- 737 (8) Jacobsen, S. B.; Pimentel-Klose, M. R. Nd Isotopic Variations in Precambrian Banded Iron  
738 Formations. *Geophys. Res. Lett.* **1988**, *15* (4), 393–396.  
739 <https://doi.org/10.1029/GL015i004p00393>.

- 740 (9) Thompson, K. J.; Kenward, P. A.; Bauer, K. W.; Warchola, T.; Gauger, T.; Martinez, R.; Simister, R.  
741 L.; Michiels, C. C.; Llorós, M.; Reinhard, C. T.; Kappler, A.; Konhauser, K. O.; Crowe, S. A.  
742 Photoferrotrophy, Deposition of Banded Iron Formations, and Methane Production in Archean  
743 Oceans. *Sci. Adv.* **2019**, *5* (11), eaav2869. <https://doi.org/10.1126/sciadv.aav2869>.
- 744 (10) Alexander, B. W.; Bau, M.; Andersson, P.; Dulski, P. Continentally-Derived Solutes in Shallow  
745 Archean Seawater: Rare Earth Element and Nd Isotope Evidence in Iron Formation from the  
746 2.9Ga Pongola Supergroup, South Africa. *Geochim. Cosmochim. Acta* **2008**, *72* (2), 378–394.  
747 <https://doi.org/10.1016/j.gca.2007.10.028>.
- 748 (11) Heard, A. W.; Aarons, S. M.; Hofmann, A.; He, X.; Ireland, T.; Bekker, A.; Qin, L.; Dauphas, N.  
749 Anoxic Continental Surface Weathering Recorded by the 2.95 Ga Denny Dalton Paleosol (Pongola  
750 Supergroup, South Africa). *Geochim. Cosmochim. Acta* **2021**, *295*, 1–23.  
751 <https://doi.org/10.1016/j.gca.2020.12.005>.
- 752 (12) Bekker, A.; Planavsky, N. J.; Krapež, B.; Rasmussen, B.; Hofmann, A.; Slack, J. F.; Rouxel, O. J.;  
753 Konhauser, K. O. 9.18 - Iron Formations: Their Origins and Implications for Ancient Seawater  
754 Chemistry. In *Treatise on Geochemistry (Second Edition)*; Holland, H. D., Turekian, K. K., Eds.;  
755 Elsevier: Oxford, 2014; pp 561–628. <https://doi.org/10.1016/B978-0-08-095975-7.00719-1>.
- 756 (13) Bekker, A.; Slack, J. F.; Planavsky, N.; Krapež, B.; Hofmann, A.; Konhauser, K. O.; Rouxel, O. J. Iron  
757 Formation: The Sedimentary Product of a Complex Interplay among Mantle, Tectonic, Oceanic,  
758 and Biospheric Processes. *Econ. Geol.* **2010**, *105* (3), 467–508.  
759 <https://doi.org/10.2113/gsecongeo.105.3.467>.
- 760 (14) Konhauser, K. O.; Planavsky, N. J.; Hardisty, D. S.; Robbins, L. J.; Warchola, T. J.; Haugaard, R.;  
761 Lalonde, S. V.; Partin, C. A.; Oonk, P. B. H.; Tsikos, H.; Lyons, T. W.; Bekker, A.; Johnson, C. M. Iron  
762 Formations: A Global Record of Neoproterozoic to Palaeoproterozoic Environmental History. *Earth-*  
763 *Sci. Rev.* **2017**, *172*, 140–177. <https://doi.org/10.1016/j.earscirev.2017.06.012>.
- 764 (15) Trendall, A. F.; Morris, R. C. *Iron-Formation: Facts and Problems*; Elsevier, 2000.
- 765 (16) Klein, C. Some Precambrian Banded Iron-Formations (BIFs) from around the World: Their Age,  
766 Geologic Setting, Mineralogy, Metamorphism, Geochemistry, and Origins. *Am. Mineral.* **2005**, *90*  
767 (10), 1473–1499. <https://doi.org/10.2138/am.2005.1871>.
- 768 (17) Cloud, P. Paleoecological Significance of the Banded Iron-Formation. *Econ. Geol.* **1973**, *68* (7),  
769 1135–1143. <https://doi.org/10.2113/gsecongeo.68.7.1135>.
- 770 (18) Braterman, P. S.; Cairns-Smith, A. G.; Sloper, R. W. Photo-Oxidation of Hydrated Fe<sup>2+</sup>—  
771 Significance for Banded Iron Formations. *Nature* **1983**, *303* (5913), 163–164.  
772 <https://doi.org/10.1038/303163a0>.
- 773 (19) Cairns-Smith, A. G. Precambrian Solution Photochemistry, Inverse Segregation, and Banded Iron  
774 Formations. *Nature* **1978**, *276* (5690), 807–808. <https://doi.org/10.1038/276807a0>.
- 775 (20) Nie, N. X.; Dauphas, N.; Greenwood, R. C. Iron and Oxygen Isotope Fractionation during Iron UV  
776 Photo-Oxidation: Implications for Early Earth and Mars. *Earth Planet. Sci. Lett.* **2017**, *458*, 179–  
777 191. <https://doi.org/10.1016/j.epsl.2016.10.035>.
- 778 (21) Kappler, A.; Pasquero, C.; Konhauser, K. O.; Newman, D. K. Deposition of Banded Iron Formations  
779 by Anoxygenic Phototrophic Fe(II)-Oxidizing Bacteria. *Geology* **2005**, *33* (11), 865–868.  
780 <https://doi.org/10.1130/G21658.1>.
- 781 (22) Konhauser, K. O.; Amskold, L.; Lalonde, S. V.; Posth, N. R.; Kappler, A.; Anbar, A. Decoupling  
782 Photochemical Fe(II) Oxidation from Shallow-Water BIF Deposition. *Earth Planet. Sci. Lett.* **2007**,  
783 *258* (1–2), 87–100. <https://doi.org/10.1016/j.epsl.2007.03.026>.
- 784 (23) Konhauser, K. O.; Hamade, T.; Raiswell, R.; Morris, R. C.; Ferris, F. G.; Southam, G.; Canfield, D. E.  
785 Could Bacteria Have Formed the Precambrian Banded Iron Formations? *Geology* **2002**, *30* (12),  
786 1079–1082. [https://doi.org/10.1130/0091-7613\(2002\)030<1079:CBHFTP>2.0.CO;2](https://doi.org/10.1130/0091-7613(2002)030<1079:CBHFTP>2.0.CO;2).

- 787 (24) Craddock, P. R.; Dauphas, N. Iron and Carbon Isotope Evidence for Microbial Iron Respiration  
788 throughout the Archean. *Earth Planet. Sci. Lett.* **2011**, *303* (1–2), 121–132.  
789 <https://doi.org/10.1016/j.epsl.2010.12.045>.
- 790 (25) Heimann, A.; Johnson, C. M.; Beard, B. L.; Valley, J. W.; Roden, E. E.; Spicuzza, M. J.; Beukes, N. J.  
791 Fe, C, and O Isotope Compositions of Banded Iron Formation Carbonates Demonstrate a Major  
792 Role for Dissimilatory Iron Reduction in ~2.5 Ga Marine Environments. *Earth Planet. Sci. Lett.*  
793 **2010**, *294* (1–2), 8–18. <https://doi.org/10.1016/j.epsl.2010.02.015>.
- 794 (26) Köhler, I.; Konhauser, K. O.; Papineau, D.; Bekker, A.; Kappler, A. Biological Carbon Precursor to  
795 Diagenetic Siderite with Spherical Structures in Iron Formations. *Nat. Commun.* **2013**, *4*, 1741.  
796 <https://doi.org/10.1038/ncomms2770>.
- 797 (27) Konhauser, K. O.; Newman, D. K.; Kappler, A. The Potential Significance of Microbial Fe(III)  
798 Reduction during Deposition of Precambrian Banded Iron Formations. *Geobiology* **2005**, *3* (3),  
799 167–177. <https://doi.org/10.1111/j.1472-4669.2005.00055.x>.
- 800 (28) Walker, J. C. G. Suboxic Diagenesis in Banded Iron Formations. *Nature* **1984**, *309* (5966), 340–342.  
801 <https://doi.org/10.1038/309340a0>.
- 802 (29) Fischer, W. W.; Knoll, A. H. An Iron Shuttle for Deepwater Silica in Late Archean and Early  
803 Paleoproterozoic Iron Formation. *GSA Bull.* **2009**, *121* (1–2), 222–235.  
804 <https://doi.org/10.1130/B26328.1>.
- 805 (30) Nims, C.; Johnson, J. E. Exploring the Secondary Mineral Products Generated by Microbial Iron  
806 Respiration in Archean Ocean Simulations. *Geobiology* **2022**, *20* (6), 743–763.  
807 <https://doi.org/10.1111/gbi.12523>.
- 808 (31) Robbins, L. J.; Funk, S. P.; Flynn, S. L.; Warchola, T. J.; Li, Z.; Lalonde, S. V.; Rostron, B. J.; Smith, A.  
809 J. B.; Beukes, N. J.; Kock, M. O. de; Heaman, L. M.; Alessi, D. S.; Konhauser, K. O. Hydrogeological  
810 Constraints on the Formation of Palaeoproterozoic Banded Iron Formations. *Nat. Geosci.* **2019**, *1*,  
811 <https://doi.org/10.1038/s41561-019-0372-0>.
- 812 (32) Dodd, M. S.; Papineau, D.; Pirajno, F.; Wan, Y.; Karhu, J. A. Minimal Biomass Deposition in Banded  
813 Iron Formations Inferred from Organic Matter and Clay Relationships. *Nat. Commun.* **2019**, *10* (1),  
814 1–13. <https://doi.org/10.1038/s41467-019-12975-z>.
- 815 (33) Bjerrum, C. J.; Canfield, D. E. Ocean Productivity before about 1.9 Gyr Ago Limited by Phosphorus  
816 Adsorption onto Iron Oxides. *Nature* **2002**, *417* (6885), 159–162.  
817 <https://doi.org/10.1038/417159a>.
- 818 (34) Jones, C.; Nomosatryo, S.; Crowe, S. A.; Bjerrum, C. J.; Canfield, D. E. Iron Oxides, Divalent  
819 Cations, Silica, and the Early Earth Phosphorus Crisis. *Geology* **2015**, *43* (2), 135–138.  
820 <https://doi.org/10.1130/G36044.1>.
- 821 (35) Konhauser, K. O.; Robbins, L. J.; Pecoits, E.; Peacock, C.; Kappler, A.; Lalonde, S. V. The Archean  
822 Nickel Famine Revisited. *Astrobiology* **2015**, *15* (10), 804–815.  
823 <https://doi.org/10.1089/ast.2015.1301>.
- 824 (36) Konhauser, K. O.; Pecoits, E.; Lalonde, S. V.; Papineau, D.; Nisbet, E. G.; Barley, M. E.; Arndt, N. T.;  
825 Zahnle, K.; Kamber, B. S. Oceanic Nickel Depletion and a Methanogen Famine before the Great  
826 Oxidation Event. *Nature* **2009**, *458* (7239), 750–753. <https://doi.org/10.1038/nature07858>.
- 827 (37) Planavsky, N. J.; Rouxel, O. J.; Bekker, A.; Lalonde, S. V.; Konhauser, K. O.; Reinhard, C. T.; Lyons,  
828 T. W. The Evolution of the Marine Phosphate Reservoir. *Nature* **2010**, *467* (7319), 1088–1090.  
829 <https://doi.org/10.1038/nature09485>.
- 830 (38) Robbins, L. J.; Lalonde, S. V.; Planavsky, N. J.; Partin, C. A.; Reinhard, C. T.; Kendall, B.; Scott, C.;  
831 Hardisty, D. S.; Gill, B. C.; Alessi, D. S.; Dupont, C. L.; Saito, M. A.; Crowe, S. A.; Poulton, S. W.;  
832 Bekker, A.; Lyons, T. W.; Konhauser, K. O. Trace Elements at the Intersection of Marine Biological  
833 and Geochemical Evolution. *Earth-Sci. Rev.* **2016**, *163*, 323–348.  
834 <https://doi.org/10.1016/j.earscirev.2016.10.013>.

- 835 (39) Johnson, J. E.; Muhling, J. R.; Cosmidis, J.; Rasmussen, B.; Templeton, A. S. Low-Fe(III) Greenalite  
836 Was a Primary Mineral From Neoproterozoic Oceans. *Geophys. Res. Lett.* **2018**, *45* (7), 3182–3192.  
837 <https://doi.org/10.1002/2017GL076311>.
- 838 (40) Rasmussen, B.; Muhling, J. R.; Krapež, B. Greenalite and Its Role in the Genesis of Early  
839 Precambrian Iron Formations – A Review. *Earth-Sci. Rev.* **2021**, 103613.  
840 <https://doi.org/10.1016/j.earscirev.2021.103613>.
- 841 (41) Rasmussen, B.; Krapež, B.; Muhling, J. R. Hematite Replacement of Iron-Bearing Precursor  
842 Sediments in the 3.46-b.y.-Old Marble Bar Chert, Pilbara Craton, Australia. *Geol. Soc. Am. Bull.*  
843 **2014**, *126* (9–10), 1245–1258. <https://doi.org/10.1130/B31049.1>.
- 844 (42) Tosca, N. J.; Jiang, C. Z.; Rasmussen, B.; Muhling, J. Products of the Iron Cycle on the Early Earth.  
845 *Free Radic. Biol. Med.* **2019**, *140*, 138–153.  
846 <https://doi.org/10.1016/j.freeradbiomed.2019.05.005>.
- 847 (43) Rasmussen, B.; Muhling, J. R. Comment on “Early Archean Biogeochemical Iron Cycling and  
848 Nutrient Availability: New Insights from a 3.5 Ga Land-Sea Transition” by Clark M. Johnson, Xin-  
849 Yuan Zheng, Tara Djokic, Martin J. Van Kranendonk, Andrew D. Czaja, Eric E. Roden, Brian L.  
850 Beard, 2022, Earth-Science Reviews, <https://doi.org/10.1016/j.earscirev.2022.103992>. *Earth-Sci.*  
851 *Rev.* **2022**, 104088. <https://doi.org/10.1016/j.earscirev.2022.104088>.
- 852 (44) Muhling, J. R.; Rasmussen, B. Widespread Deposition of Greenalite to Form Banded Iron  
853 Formations before the Great Oxidation Event. *Precambrian Res.* **2020**, 105619.  
854 <https://doi.org/10.1016/j.precamres.2020.105619>.
- 855 (45) Rasmussen, B.; Muhling, J. R.; Tosca, N. J.; Tsikos, H. Evidence for Anoxic Shallow Oceans at 2.45  
856 Ga: Implications for the Rise of Oxygenic Photosynthesis. *Geology* **2019**.  
857 <https://doi.org/10.1130/G46162.1>.
- 858 (46) Rasmussen, B.; Krapež, B.; Muhling, J. R.; Suvorova, A. Precipitation of Iron Silicate Nanoparticles  
859 in Early Precambrian Oceans Marks Earth’s First Iron Age. *Geology* **2015**, *43* (4), 303–306.  
860 <https://doi.org/10.1130/G36309.1>.
- 861 (47) Rasmussen, B.; Krapež, B.; Meier, D. B. Replacement Origin for Hematite in 2.5 Ga Banded Iron  
862 Formation: Evidence for Postdepositional Oxidation of Iron-Bearing Minerals. *Geol. Soc. Am. Bull.*  
863 **2014**, B30944.1. <https://doi.org/10.1130/B30944.1>.
- 864 (48) Rasmussen, B.; Muhling, J. R.; Suvorova, A.; Krapež, B. Dust to Dust: Evidence for the Formation  
865 of “Primary” Hematite Dust in Banded Iron Formations via Oxidation of Iron Silicate  
866 Nanoparticles. *Precambrian Res.* **2016**, *284*, 49–63.  
867 <https://doi.org/10.1016/j.precamres.2016.07.003>.
- 868 (49) Frost, C. D.; von Blanckenburg, F.; Schoenberg, R.; Frost, B. R.; Swapp, S. M. Preservation of Fe  
869 Isotope Heterogeneities during Diagenesis and Metamorphism of Banded Iron Formation.  
870 *Contrib. Mineral. Petrol.* **2006**, *153* (2), 211. <https://doi.org/10.1007/s00410-006-0141-0>.
- 871 (50) Dauphas, N.; John, S. G.; Rouxel, O. Iron Isotope Systematics. *Rev. Mineral. Geochem.* **2017**, *82*  
872 (1), 415–510. <https://doi.org/10.1515/9783110545630-012>.
- 873 (51) Heard, A. W.; Dauphas, N. Constraints on the Coevolution of Oxic and Sulfidic Ocean Iron Sinks  
874 from Archean–Paleoproterozoic Iron Isotope Records. *Geology* **2020**, *48* (4), 358–362.  
875 <https://doi.org/10.1130/G46951.1>.
- 876 (52) Dauphas, N.; Cates, N. L.; Mojzsis, S. J.; Busigny, V. Identification of Chemical Sedimentary  
877 Protoliths Using Iron Isotopes in the > 3750 Ma Nuvvuagittuq Supracrustal Belt, Canada. *Earth*  
878 *Planet. Sci. Lett.* **2007**, *254* (3–4), 358–376. <https://doi.org/10.1016/j.epsl.2006.11.042>.
- 879 (53) Dauphas, N.; van Zuilen, M.; Busigny, V.; Lepland, A.; Wadhwa, M.; Janney, P. E. Iron Isotope,  
880 Major and Trace Element Characterization of Early Archean Supracrustal Rocks from SW  
881 Greenland: Protolith Identification and Metamorphic Overprint. *Geochim. Cosmochim. Acta* **2007**,  
882 *71* (19), 4745–4770. <https://doi.org/10.1016/j.gca.2007.07.019>.

- 883 (54) Dauphas, N.; Zuilen, M. van; Wadhwa, M.; Davis, A. M.; Marty, B.; Janney, P. E. Clues from Fe  
884 Isotope Variations on the Origin of Early Archean BIFs from Greenland. *Science* **2004**, *306* (5704),  
885 2077–2080. <https://doi.org/10.1126/science.1104639>.
- 886 (55) Beard, B. L.; Handler, R. M.; Scherer, M. M.; Wu, L.; Czaja, A. D.; Heimann, A.; Johnson, C. M. Iron  
887 Isotope Fractionation between Aqueous Ferrous Iron and Goethite. *Earth Planet. Sci. Lett.* **2010**,  
888 *295* (1), 241–250. <https://doi.org/10.1016/j.epsl.2010.04.006>.
- 889 (56) Bullen, T. D.; White, A. F.; Childs, C. W.; Vivit, D. V.; Schulz, M. S. Demonstration of Significant  
890 Abiotic Iron Isotope Fractionation in Nature. *Geology* **2001**, *29* (8), 699–702.  
891 [https://doi.org/10.1130/0091-7613\(2001\)029<0699:DOSAII>2.0.CO;2](https://doi.org/10.1130/0091-7613(2001)029<0699:DOSAII>2.0.CO;2).
- 892 (57) Croal, L. R.; Johnson, C. M.; Beard, B. L.; Newman, D. K. Iron Isotope Fractionation by Fe(II)-  
893 Oxidizing Photoautotrophic Bacteria 1. *Geochim. Cosmochim. Acta* **2004**, *68* (6), 1227–1242.  
894 <https://doi.org/10.1016/j.gca.2003.09.011>.
- 895 (58) Skulan, J. L.; Beard, B. L.; Johnson, C. M. Kinetic and Equilibrium Fe Isotope Fractionation between  
896 Aqueous Fe(III) and Hematite. *Geochim. Cosmochim. Acta* **2002**, *66* (17), 2995–3015.  
897 [https://doi.org/10.1016/S0016-7037\(02\)00902-X](https://doi.org/10.1016/S0016-7037(02)00902-X).
- 898 (59) Wu, L.; Beard, B. L.; Roden, E. E.; Johnson, C. M. Stable Iron Isotope Fractionation Between  
899 Aqueous Fe(II) and Hydrous Ferric Oxide. *Environ. Sci. Technol.* **2011**, *45* (5), 1847–1852.  
900 <https://doi.org/10.1021/es103171x>.
- 901 (60) Wiesli, R. A.; Beard, B. L.; Johnson, C. M. Experimental Determination of Fe Isotope Fractionation  
902 between Aqueous Fe(II), Siderite and “Green Rust” in Abiotic Systems. *Chem. Geol.* **2004**, *211* (3),  
903 343–362. <https://doi.org/10.1016/j.chemgeo.2004.07.002>.
- 904 (61) Li, W.; Czaja, A. D.; Van Kranendonk, M. J.; Beard, B. L.; Roden, E. E.; Johnson, C. M. An Anoxic,  
905 Fe(II)-Rich, U-Poor Ocean 3.46 Billion Years Ago. *Geochim. Cosmochim. Acta* **2013**, *120*, 65–79.  
906 <https://doi.org/10.1016/j.gca.2013.06.033>.
- 907 (62) Blanchard, M.; Dauphas, N.; Hu, M. Y.; Roskosz, M.; Alp, E. E.; Golden, D. C.; Sio, C. K.; Tissot, F. L.  
908 H.; Zhao, J.; Gao, L.; Morris, R. V.; Fornace, M.; Floris, A.; Lazzeri, M.; Balan, E. Reduced Partition  
909 Function Ratios of Iron and Oxygen in Goethite. *Geochim. Cosmochim. Acta* **2015**, *151*, 19–33.  
910 <https://doi.org/10.1016/j.gca.2014.12.006>.
- 911 (63) Dauphas, N.; Roskosz, M.; Alp, E. E.; Golden, D. C.; Sio, C. K.; Tissot, F. L. H.; Hu, M. Y.; Zhao, J.;  
912 Gao, L.; Morris, R. V. A General Moment NRIXS Approach to the Determination of Equilibrium Fe  
913 Isotopic Fractionation Factors: Application to Goethite and Jarosite. *Geochim. Cosmochim. Acta*  
914 **2012**, *94*, 254–275. <https://doi.org/10.1016/j.gca.2012.06.013>.
- 915 (64) Nie, N. X.; Dauphas, N.; Alp, E. E.; Zeng, H.; Sio, C. K.; Hu, J. Y.; Chen, X.; Aarons, S. M.; Zhang, Z.;  
916 Tian, H.-C.; Wang, D.; Prissel, K. B.; Greer, J.; Bi, W.; Hu, M. Y.; Zhao, J.; Shahar, A.; Roskosz, M.;  
917 Teng, F.-Z.; Krawczynski, M. J.; Heck, P. R.; Spear, F. S. Iron, Magnesium, and Titanium Isotopic  
918 Fractionations between Garnet, Ilmenite, Fayalite, Biotite, and Tourmaline: Results from NRIXS,  
919 Ab Initio, and Study of Mineral Separates from the Moosilauke Metapelite. *Geochim. Cosmochim.*  
920 *Acta* **2021**. <https://doi.org/10.1016/j.gca.2021.03.014>.
- 921 (65) Schauble, E. A.; Rossman, G. R.; Taylor, H. P. Theoretical Estimates of Equilibrium Fe-Isotope  
922 Fractionations from Vibrational Spectroscopy. *Geochim. Cosmochim. Acta* **2001**, *65* (15), 2487–  
923 2497. [https://doi.org/10.1016/S0016-7037\(01\)00600-7](https://doi.org/10.1016/S0016-7037(01)00600-7).
- 924 (66) Johnson, C. M.; Skulan, J. L.; Beard, B. L.; Sun, H.; Nealson, K. H.; Braterman, P. S. Isotopic  
925 Fractionation between Fe(III) and Fe(II) in Aqueous Solutions. *Earth Planet. Sci. Lett.* **2002**, *195*  
926 (1–2), 141–153. [https://doi.org/10.1016/S0012-821X\(01\)00581-7](https://doi.org/10.1016/S0012-821X(01)00581-7).
- 927 (67) Welch, S. A.; Beard, B. L.; Johnson, C. M.; Braterman, P. S. Kinetic and Equilibrium Fe Isotope  
928 Fractionation between Aqueous Fe(II) and Fe(III). *Geochim. Cosmochim. Acta* **2003**, *67* (22),  
929 4231–4250. [https://doi.org/10.1016/S0016-7037\(03\)00266-7](https://doi.org/10.1016/S0016-7037(03)00266-7).

- 930 (68) Anbar, A. D.; Jarzecki, A. A.; Spiro, T. G. Theoretical Investigation of Iron Isotope Fractionation  
931 between Fe(H<sub>2</sub>O)<sub>6</sub><sup>3+</sup> and Fe(H<sub>2</sub>O)<sub>6</sub><sup>2+</sup>: Implications for Iron Stable Isotope Geochemistry.  
932 *Geochim. Cosmochim. Acta* **2005**, *69* (4), 825–837. <https://doi.org/10.1016/j.gca.2004.06.012>.
- 933 (69) Domagal-Goldman, S. D.; Kubicki, J. D. Density Functional Theory Predictions of Equilibrium  
934 Isotope Fractionation of Iron Due to Redox Changes and Organic Complexation. *Geochim.*  
935 *Cosmochim. Acta* **2008**, *72* (21), 5201–5216. <https://doi.org/10.1016/j.gca.2008.05.066>.
- 936 (70) Hill, P. S.; Schauble, E. A. Modeling the Effects of Bond Environment on Equilibrium Iron Isotope  
937 Fractionation in Ferric Aquo-Chloro Complexes. *Geochim. Cosmochim. Acta* **2008**, *72* (8), 1939–  
938 1958. <https://doi.org/10.1016/j.gca.2007.12.023>.
- 939 (71) Ottonello, G.; Zuccolini, M. V. Ab-Initio Structure, Energy and Stable Fe Isotope Equilibrium  
940 Fractionation of Some Geochemically Relevant H–O–Fe Complexes. *Geochim. Cosmochim. Acta*  
941 **2009**, *73* (21), 6447–6469. <https://doi.org/10.1016/j.gca.2009.06.034>.
- 942 (72) Rustad, J. R.; Dixon, D. A. Prediction of Iron-Isotope Fractionation Between Hematite (α-Fe<sub>2</sub>O<sub>3</sub>)  
943 and Ferric and Ferrous Iron in Aqueous Solution from Density Functional Theory. *J. Phys. Chem. A*  
944 **2009**, *113* (44), 12249–12255. <https://doi.org/10.1021/jp9065373>.
- 945 (73) Blanchard, M.; Poitrasson, F.; Méheut, M.; Lazzeri, M.; Mauri, F.; Balan, E. Iron Isotope  
946 Fractionation between Pyrite (FeS<sub>2</sub>), Hematite (Fe<sub>2</sub>O<sub>3</sub>) and Siderite (FeCO<sub>3</sub>): A First-Principles  
947 Density Functional Theory Study. *Geochim. Cosmochim. Acta* **2009**, *73* (21), 6565–6578.  
948 <https://doi.org/10.1016/j.gca.2009.07.034>.
- 949 (74) Crosby; Roden Eric E.; Johnson Clark M.; Beard Brian L. The Mechanisms of Iron Isotope  
950 Fractionation Produced during Dissimilatory Fe(III) Reduction by *Shewanella Putrefaciens* and  
951 *Geobacter Sulfurreducens*. *Geobiology* **2007**, *5* (2), 169–189. <https://doi.org/10.1111/j.1472-4669.2007.00103.x>.
- 953 (75) Swanner, E. D.; Bayer, T.; Wu, W.; Hao, L.; Obst, M.; Sundman, A.; Byrne, J. M.; Michel, F. M.;  
954 Kleinhanns, I. C.; Kappler, A.; Schoenberg, R. Iron Isotope Fractionation during Fe(II) Oxidation  
955 Mediated by the Oxygen-Producing Marine Cyanobacterium *Synechococcus* PCC 7002. *Environ.*  
956 *Sci. Technol.* **2017**. <https://doi.org/10.1021/acs.est.6b05833>.
- 957 (76) Guggenheim, S.; Bailey, S. W.; Eggleton, R. A.; Wilkes, P. STRUCTURAL ASPECTS OF GREENALITE  
958 AND RELATED MINERALS. *Can. Mineral.* **1982**, *20*, 1–18.
- 959 (77) Schwertmann, U.; Cornell, R. M. Ferrihydrite. In *Iron Oxides in the Laboratory*; John Wiley & Sons,  
960 Ltd, 2000; pp 103–112. <https://doi.org/10.1002/9783527613229.ch08>.
- 961 (78) Hammersley, A. P. FIT2D: A Multi-Purpose Data Reduction, Analysis and Visualization Program. *J.*  
962 *Appl. Crystallogr.* **2016**, *49* (2), 646–652. <https://doi.org/10.1107/S1600576716000455>.
- 963 (79) Janney, D. E.; Cowley, J. M.; Buseck, P. R. Transmission Electron Microscopy of Synthetic 2- and 6-  
964 Line Ferrihydrite. *Clays Clay Miner.* **2000**, *48* (1), 111–119.  
965 <https://doi.org/10.1346/CCMN.2000.0480114>.
- 966 (80) Seto, M.; Yoda, Y.; Kikuta, S.; Zhang, X. W.; Ando, M. Observation of Nuclear Resonant Scattering  
967 Accompanied by Phonon Excitation Using Synchrotron Radiation. *Phys. Rev. Lett.* **1995**, *74* (19),  
968 3828–3831. <https://doi.org/10.1103/PhysRevLett.74.3828>.
- 969 (81) Sturhahn, W.; Toellner, T. S.; Alp, E. E.; Zhang, X.; Ando, M.; Yoda, Y.; Kikuta, S.; Seto, M.; Kimball,  
970 C. W.; Dabrowski, B. Phonon Density of States Measured by Inelastic Nuclear Resonant  
971 Scattering. *Phys. Rev. Lett.* **1995**, *74* (19), 3832–3835.  
972 <https://doi.org/10.1103/PhysRevLett.74.3832>.
- 973 (82) Hu, M. Y.; Toellner, T. S.; Dauphas, N.; Alp, E. E.; Zhao, J. Moments in Nuclear Resonant Inelastic  
974 X-Ray Scattering and Their Applications. *Phys. Rev. B* **2013**, *87* (6), 064301.  
975 <https://doi.org/10.1103/PhysRevB.87.064301>.

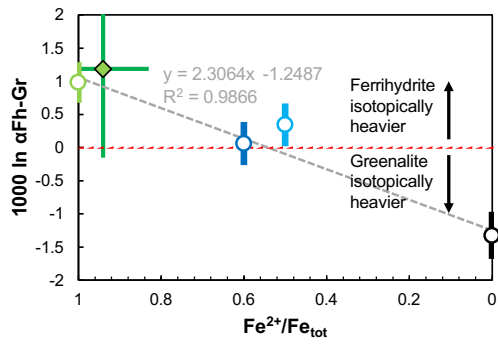
- 976 (83) Polyakov, V. B.; Mineev, S. D. The Use of Mössbauer Spectroscopy in Stable Isotope  
977 Geochemistry. *Geochim. Cosmochim. Acta* **2000**, *64* (5), 849–865. [https://doi.org/10.1016/S0016-](https://doi.org/10.1016/S0016-7037(99)00329-4)  
978 7037(99)00329-4.
- 979 (84) Dauphas, N.; Hu, M. Y.; Baker, E. M.; Hu, J.; Tissot, F. L. H.; Alp, E. E.; Roskosz, M.; Zhao, J.; Bi, W.;  
980 Liu, J.; Lin, J.-F.; Nie, N. X.; Heard, A. SciPhon: A Data Analysis Software for Nuclear Resonant  
981 Inelastic X-Ray Scattering with Applications to Fe, Kr, Sn, Eu and Dy. *J. Synchrotron Radiat.* **2018**,  
982 *25* (5), 1581–1599. <https://doi.org/10.1107/S1600577518009487>.
- 983 (85) Sturhahn, W. CONUSS and PHOENIX: Evaluation of Nuclear Resonant Scattering Data. *Hyperfine*  
984 *Interact.* **2000**, *125* (1), 149–172. <https://doi.org/10.1023/A:1012681503686>.
- 985 (86) van Bürck, U.; Siddons, D. P.; Hastings, J. B.; Bergmann, U.; Hollatz, R. Nuclear Forward Scattering  
986 of Synchrotron Radiation. *Phys. Rev. B* **1992**, *46* (10), 6207–6211.  
987 <https://doi.org/10.1103/PhysRevB.46.6207>.
- 988 (87) Alp, E. E.; Sturhahn, W.; Toellner, T. S. Synchrotron Mossbauer Spectroscopy of Powder Samples.  
989 *Nucl. Instrum. Methods Phys. Res. Sect. B Beam Interact. Mater. At.* **1995**, *97* (1–4), 526–529.  
990 [https://doi.org/10.1016/0168-583X\(94\)00743-8](https://doi.org/10.1016/0168-583X(94)00743-8).
- 991 (88) Evans, B. W.; Dyar, M. D.; Kuehner, S. M. Implications of Ferrous and Ferric Iron in Antigorite. *Am.*  
992 *Mineral.* **2012**, *97* (1), 184–196. <https://doi.org/10.2138/am.2012.3926>.
- 993 (89) Tutolo, B. M.; Seyfried, W. E.; Tosca, N. J. A Seawater Throttle on H<sub>2</sub> Production in Precambrian  
994 Serpentinizing Systems. *Proc. Natl. Acad. Sci.* **2020**. <https://doi.org/10.1073/pnas.1921042117>.
- 995 (90) Tutolo, B. M.; Evans, B. W.; Kuehner, S. M. Serpentine–Hisingerite Solid Solution in Altered  
996 Ferroan Peridotite and Olivine Gabbro. *Minerals* **2019**, *9* (1), 47.  
997 <https://doi.org/10.3390/min9010047>.
- 998 (91) Michel, F. M.; Ehm, L.; Antao, S. M.; Lee, P. L.; Chupas, P. J.; Liu, G.; Strongin, D. R.; Schoonen, M.  
999 A. A.; Phillips, B. L.; Parise, J. B. The Structure of Ferrihydrite, a Nanocrystalline Material. *Science*  
1000 **2007**, *316* (5832), 1726–1729. <https://doi.org/10.1126/science.1142525>.
- 1001 (92) Drits, V. A.; Sakharov, B. A.; Salyn, A. L.; Manceau, A. Structural Model for Ferrihydrite. *Clay*  
1002 *Miner.* **1993**, *28* (2), 185–207. <https://doi.org/10.1180/claymin.1993.028.2.02>.
- 1003 (93) Sassi, M.; Chaka, A. M.; Rosso, K. M. Ab Initio Thermodynamics Reveals the Nanocomposite  
1004 Structure of Ferrihydrite. *Commun. Chem.* **2021**, *4* (1), 1–10. [https://doi.org/10.1038/s42004-](https://doi.org/10.1038/s42004-021-00562-7)  
1005 021-00562-7.
- 1006 (94) Giannozzi, P.; Baroni, S.; Bonini, N.; Calandra, M.; Car, R.; Cavazzoni, C.; Ceresoli, D.; Chiarotti, G.  
1007 L.; Cococcioni, M.; Dabo, I.; Dal Corso, A.; de Gironcoli, S.; Fabris, S.; Fratesi, G.; Gebauer, R.;  
1008 Gerstmann, U.; Gougoussis, C.; Kokalj, A.; Lazzeri, M.; Martin-Samos, L.; Marzari, N.; Mauri, F.;  
1009 Mazzarello, R.; Paolini, S.; Pasquarello, A.; Paulatto, L.; Sbraccia, C.; Scandolo, S.; Sclauzero, G.;  
1010 Seitsonen, A. P.; Smogunov, A.; Umari, P.; Wentzcovitch, R. M. QUANTUM ESPRESSO: A Modular  
1011 and Open-Source Software Project for Quantum Simulations of Materials. *J. Phys. Condens.*  
1012 *Matter Inst. Phys. J.* **2009**, *21* (39), 395502. <https://doi.org/10.1088/0953-8984/21/39/395502>.
- 1013 (95) Perdew, J. P.; Burke, K.; Ernzerhof, M. Generalized Gradient Approximation Made Simple. *Phys.*  
1014 *Rev. Lett.* **1996**, *77* (18), 3865–3868. <https://doi.org/10.1103/PhysRevLett.77.3865>.
- 1015 (96) Garrity, K. F.; Bennett, J. W.; Rabe, K. M.; Vanderbilt, D. Pseudopotentials for High-Throughput  
1016 DFT Calculations. *Comput. Mater. Sci.* **2014**, *81*, 446–452.  
1017 <https://doi.org/10.1016/j.commatsci.2013.08.053>.
- 1018 (97) Monkhorst, H. J.; Pack, J. D. Special Points for Brillouin-Zone Integrations. *Phys. Rev. B* **1976**, *13*  
1019 (12), 5188–5192. <https://doi.org/10.1103/PhysRevB.13.5188>.
- 1020 (98) Pinney, N.; Kubicki, J. D.; Middlemiss, D. S.; Grey, C. P.; Morgan, D. Density Functional Theory  
1021 Study of Ferrihydrite and Related Fe-Oxyhydroxides. *Chem. Mater.* **2009**, *21* (24), 5727–5742.  
1022 <https://doi.org/10.1021/cm9023875>.

- 1023 (99) Coey, J. M. D.; Ballet, O.; Moukarika, A.; Soubeyroux, J. L. Magnetic Properties of Sheet Silicates;  
 1024 1:1 Layer Minerals. *Phys. Chem. Miner.* **1981**, *7* (3), 141–148.  
 1025 <https://doi.org/10.1007/BF00308232>.
- 1026 (100) Cococcioni, M.; de Gironcoli, S. Linear Response Approach to the Calculation of the Effective  
 1027 Interaction Parameters in the  $\mathit{LDA}+\mathit{U}$  Method. *Phys. Rev. B* **2005**, *71* (3),  
 1028 035105. <https://doi.org/10.1103/PhysRevB.71.035105>.
- 1029 (101) Kulik, H. J.; Cococcioni, M.; Scherlis, D. A.; Marzari, N. Density Functional Theory in Transition-  
 1030 Metal Chemistry: A Self-Consistent Hubbard  $U$  Approach. *Phys. Rev. Lett.* **2006**, *97* (10),  
 1031 103001. <https://doi.org/10.1103/PhysRevLett.97.103001>.
- 1032 (102) Blanchard, M.; Balan, E.; Schauble, E. A. Equilibrium Fractionation of Non-Traditional Isotopes: A  
 1033 Molecular Modeling Perspective. *Rev. Mineral. Geochem.* **2017**, *82* (1), 27–63.  
 1034 <https://doi.org/10.2138/rmg.2017.82.2>.
- 1035 (103) Baroni, S.; de Gironcoli, S.; Dal Corso, A.; Giannozzi, P. Phonons and Related Crystal Properties  
 1036 from Density-Functional Perturbation Theory. *Rev. Mod. Phys.* **2001**, *73* (2), 515–562.  
 1037 <https://doi.org/10.1103/RevModPhys.73.515>.
- 1038 (104) Aarons, S. M.; Dauphas, N.; Blanchard, M.; Zeng, H.; Nie, N. X.; Johnson, A. C.; Greber, N. D.;  
 1039 Hopp, T. Clues from Ab Initio Calculations on Titanium Isotopic Fractionation in Tholeiitic and  
 1040 Calc-Alkaline Magma Series. *ACS Earth Space Chem.* **2021**, *5* (9), 2466–2480.  
 1041 <https://doi.org/10.1021/acsearthspacechem.1c00172>.
- 1042 (105) Dauphas, N.; Nie, N. X.; Blanchard, M.; Zhang, Z. J.; Zeng, H.; Hu, J. Y.; Meheut, M.; Visscher, C.;  
 1043 Canup, R.; Hopp, T. The Extent, Nature, and Origin of K and Rb Depletions and Isotopic  
 1044 Fractionations in Earth, the Moon, and Other Planetary Bodies. *Planet. Sci. J.* **2022**, *3* (2), 29.  
 1045 <https://doi.org/10.3847/PSJ/ac2e09>.
- 1046 (106) Gruner, J. W. The Structure and Chemical Composition of Greenalite. *Am. Mineral.* **1936**, *21* (7),  
 1047 449–455.
- 1048 (107) Lee, S.; Xu, H. One-Step Route Synthesis of Siliceous Six-Line Ferrihydrite: Implication for the  
 1049 Formation of Natural Ferrihydrite. *ACS Earth Space Chem.* **2019**, *3* (4), 503–509.  
 1050 <https://doi.org/10.1021/acsearthspacechem.8b00179>.
- 1051 (108) Beard, B. L.; Johnson, C. M.; Damm, K. L. V.; Poulson, R. L. Iron Isotope Constraints on Fe Cycling  
 1052 and Mass Balance in Oxygenated Earth Oceans. *Geology* **2003**, *31* (7), 629–632.  
 1053 [https://doi.org/10.1130/0091-7613\(2003\)031<0629:IICOFC>2.0.CO;2](https://doi.org/10.1130/0091-7613(2003)031<0629:IICOFC>2.0.CO;2).
- 1054 (109) Severmann, S.; Johnson, C. M.; Beard, B. L.; German, C. R.; Edmonds, H. N.; Chiba, H.; Green, D. R.  
 1055 H. The Effect of Plume Processes on the Fe Isotope Composition of Hydrothermally Derived Fe in  
 1056 the Deep Ocean as Inferred from the Rainbow Vent Site, Mid-Atlantic Ridge, 36°14'N. *Earth*  
 1057 *Planet. Sci. Lett.* **2004**, *225* (1), 63–76. <https://doi.org/10.1016/j.epsl.2004.06.001>.
- 1058 (110) Johnson, C. M.; Zheng, X.-Y.; Djokic, T.; Van Kranendonk, M. J.; Czaja, A. D.; Roden, E. E.; Beard, B.  
 1059 L. Early Archean Biogeochemical Iron Cycling and Nutrient Availability: New Insights from a 3.5 Ga  
 1060 Land-Sea Transition. *Earth-Sci. Rev.* **2022**, *228*, 103992.  
 1061 <https://doi.org/10.1016/j.earscirev.2022.103992>.
- 1062 (111) Heard, A. W.; Bekker, A.; Kovalick, A.; Tsikos, H.; Ireland, T.; Dauphas, N. Oxygen Production and  
 1063 Rapid Iron Oxidation in Stromatolites Immediately Predating the Great Oxidation Event. *Earth*  
 1064 *Planet. Sci. Lett.* **2022**, *582*, 117416. <https://doi.org/10.1016/j.epsl.2022.117416>.
- 1065 (112) Hiebert, R. S.; Bekker, A.; Houlé, M. G.; Rouxel, O. J. Depositional Setting of the Late Archean Fe  
 1066 Oxide- and Sulfide-Bearing Chert and Graphitic Argillite in the Shaw Dome, Abitibi Greenstone  
 1067 Belt, Canada. *Precambrian Res.* **2018**, *311*, 98–116.  
 1068 <https://doi.org/10.1016/j.precamres.2018.04.004>.
- 1069 (113) Nie, N. X.; Dauphas, N.; Villalon, K. L.; Liu, N.; Heard, A. W.; Morris, R. V.; Mertzman, S. A. Iron  
 1070 Isotopic and Chemical Tracing of Basalt Alteration and Hematite Spherule Formation in Hawaii: A



1071 Prospective Study for Mars. *Earth Planet. Sci. Lett.* **2020**, *544*, 116385.  
1072 <https://doi.org/10.1016/j.epsl.2020.116385>.  
1073 (114) Planavsky, N. J.; Asael, D.; Hofmann, A.; Reinhard, C. T.; Lalonde, S. V.; Knudsen, A.; Wang, X.;  
1074 Ossa Ossa, F.; Pecoits, E.; Smith, A. J. B.; Beukes, N. J.; Bekker, A.; Johnson, T. M.; Konhauser, K.  
1075 O.; Lyons, T. W.; Rouxel, O. J. Evidence for Oxygenic Photosynthesis Half a Billion Years before the  
1076 Great Oxidation Event. *Nat. Geosci.* **2014**, *7* (4), 283–286. <https://doi.org/10.1038/ngeo2122>.  
1077 (115) Thibon, F.; Blichert-Toft, J.; Tsikos, H.; Foden, J.; Albalat, E.; Albarede, F. Dynamics of Oceanic Iron  
1078 Prior to the Great Oxygenation Event. *Earth Planet. Sci. Lett.* **2019**, *506*, 360–370.  
1079 <https://doi.org/10.1016/j.epsl.2018.11.016>.  
1080 (116) Ingalls, M.; Grotzinger, J. P.; Present, T.; Rasmussen, B.; Fischer, W. W. Carbonate-Associated  
1081 Phosphate (CAP) Indicates Elevated Phosphate Availability in Neoproterozoic Shallow Marine  
1082 Environments. *Geophys. Res. Lett.* **2022**, *49* (6), e2022GL098100.  
1083 <https://doi.org/10.1029/2022GL098100>.  
1084 (117) Rasmussen, B.; Muhling, J. R.; Suvorova, A.; Fischer, W. W. Apatite Nanoparticles in 3.46–2.46 Ga  
1085 Iron Formations: Evidence for Phosphorus-Rich Hydrothermal Plumes on Early Earth. *Geology*  
1086 **2021**, *49* (6), 647–651. <https://doi.org/10.1130/G48374.1>.  
1087 (118) Reinhard, C. T.; Planavsky, N. J.; Gill, B. C.; Ozaki, K.; Robbins, L. J.; Lyons, T. W.; Fischer, W. W.;  
1088 Wang, C.; Cole, D. B.; Konhauser, K. O. Evolution of the Global Phosphorus Cycle. *Nature* **2017**,  
1089 *541* (7637), 386–389. <https://doi.org/10.1038/nature20772>.  
1090  
1091

1092 FOR TOC ONLY



1093